Dynamics of Deep Thermocline Jets in the POLYMODE Region

NADIA PINARDI AND ALLAN R. ROBINSON

Center for Earth and Planetary Physics, Harvard University, Cambridge, MA 02138

(Manuscript received 22 January 1986, in final form 5 January 1987)

ABSTRACT

We present the study of a series of very energetic events, which occur in the 360 days of the Polymode Synoptic Dynamics Experiment dataset. The method consists of the assimilation of data by a quasi-geostrophic open boundary model so that dynamically adjusted fields are produced. They are used to study local dynamical vorticity and energy balances during 20 to 30 day benchmark forecast experiments.

The data and forecasts show the presence of strong jets at the thermocline levels (100–1400 meters), which intensify via a process of baroclinic conversion of available gravitational energy into kinetic energy. The formation, together with strengthening, of these jets is explained in terms of amplifying short-scale baroclinic waves growing along the sheared borders of larger eddies. Associated with the local steepening of the frontal areas, there is a cyclone development process that results from the growth of these short baroclinic waves. Thus, the area at the southern boundary of the Gulf Stream recirculation gyre is found to be a region of in situ baroclinic energy conversions: the time scale of the process is 30 days and the short length-scale waves amplify in a region of the order of a hundred kilometers.

1. Introduction

In this paper we describe the energetics of a few strong mesoscale jets and eddies in the western North Atlantic open ocean regions. The study of the local dynamics of mesoscale eddies in the North Atlantic Ocean has been the subject of intensive measurement programs in the past decade. Starting with MODE in an area southwest of Bermuda and following with POLYMODE, oceanographers have accumulated data and experience in the modeling and the understanding of the three-dimensional structure of the eddy field, its statistical properties and the role of the eddies in the general circulation. The most extensive experiment was POLYMODE (Robinson, 1982), a joint U.S.–U.S.S.R. program which encompassed a Synoptic Dynamical Experiment (SDE), a Local Dynamics Experiment (LDE), and a statistical geographical experiment. The scientific objectives of these three different experiments were respectively to describe and map the synoptic structure of the variability in a region containing one or more eddies for several eddy cycles, to yield estimates of the local dynamical balances in the midocean eddy regime, and to achieve a statistical description of the eddy field throughout the western North Atlantic.

Here we treat some of the findings of the POLYMODE SDE which was centered at (29°N, 70°W), on the southern edge of the Gulf Stream recirculation gyre (see Fig. 1). The SDE measurements considered here are part of the extensive XBT surveys over a 500×500 km^2 area, and USSR current meter measurements, which covered the inner 300×300 km^2 of the region. The data were collected in 1977 and 1978. We present an attempt to explain the local dynamics of the mesoscale eddies in the POLYMODE SDE region via data assimilation in the Harvard quasi-geostrophic open ocean model (Miller et al., 1983). The melding of data and model dynamics (Robinson and Leslie, 1985) produces fields which contain the observed features and which can be quantitatively physically analyzed. The use of the model to interpolate dynamically the data allows a self-consistent estimation of instantaneous vorticity and energy balances necessary to study the local mesoscale processes (Pinardi and Robinson, 1986).

A striking feature of the mesoscale-synoptic variability in the POLYMODE areas is the presence of strong thermocline jets (McWilliams et al., 1983a, 1986; Hua et al., 1986) and small cyclonic eddies associated with them (Shen et al., 1986). Here, a 360 day time series of quasi-geostrophic fields is examined and three major high energy periods are selected for study, which contain the intensification and/or formation of strong jets and eddies. Their development is studied in terms of local energy transport and conversion processes. Deep thermocline finite amplitude baroclinic processes occur rooted in strongly inhomogeneous local temperature gradients on the borders of large eddies.

The MODE measurements showed that the time scale of the energy containing variability in the region lies between 150 and 50 days and the correlation length scales between 150 and 50 km (Mode Group, 1978). Bryden and Fofonoff (1977) have shown that geostrophy and nondivergence are established to within 10%,

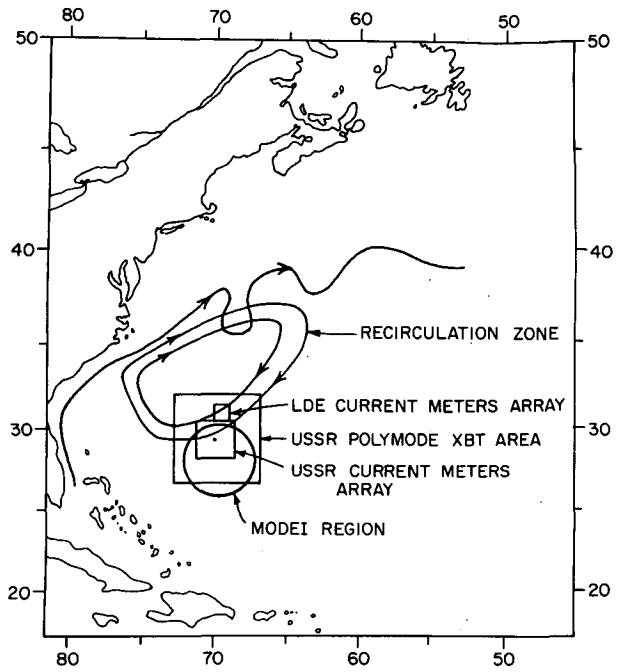

FIG. 1. The large-scale environment of the Gulf Stream recirculation zone. The MODE-I and POLYMODE LDE, SDE areas are shown.

the expected instrumental error. Furthermore, McWilliams (1976), mapping quasi-geostrophic potential vorticity balances from objectively analyzed pressure fields, has shown that the dynamics in the upper thermocline is highly nonlinear over the ten-day time scale. The POLYMODE LDE measurements have confirmed part of the findings in the MODE area, although the energy partition in time and horizontal/vertical scales is different (Owens et al., 1982; Bryden, 1982; McWilliams, 1983b). The LDE studies, both for the temporal length of the measurement survey and the accurate spatial coverage, have given estimates for the mean heat, vorticity and momentum balances. They show important local energy conversions in the mesoscale eddy field, substantial eddy flux divergences in the mean balances and the possibility for wave propagation and baroclinic instability. In this paper we show the local signature of wave propagation and baroclinic conversions which produce changes in the structure of the eddies locally. The time scale of these processes is of the order of 30 days and the spatial scales of the energy containing variability is of the order of a few hundred kilometers or smaller.

In section 2, we describe the model and the dataset. In section 3, the analysis procedure to obtain quasi-geostrophic pressure fields is explained. In section 4, the kinetic and barotropic-baroclinic kinetic energy time series for the 360 day dataset is presented, and the intense thermocline jet periods are introduced. In section 5 we describe the result of the dynamical interpolation of the data fields. In section 6, the Energy and Vorticity Analysis (EVA) of the events is displayed and interpreted.

2. The dynamical model and the dataset

The Harvard open ocean quasi-geostrophic model integrates the equations in the form

$$\partial_t(\nabla^2\psi) + \Gamma^2\partial_t(\sigma\psi_z)_z = -\alpha\mathbf{v}\cdot\nabla(\nabla^2\psi) - \alpha\Gamma^2\mathbf{v}\cdot\nabla(\sigma\psi_z)_z - \beta\psi_x + F \quad (1a)$$

$$\dot{R} + \dot{T} = \Delta F_R + \Delta F_T + \Delta F_P + F \quad (1b)$$

where all the parameters α, β, Γ^2, σ are explained in Table 1, $\mathbf{v} = +\mathbf{k}\times\nabla\psi$, $\mathbf{k}$ is the unit vector in the vertical direction and F is the model parameterization of the dissipation done by a Shapiro filter operation on the vorticity (Shapiro, 1970). Hereafter we will use the symbol "∂" and/or the subscript to indicate partial differentiation. Equation (1b) is the symbolic representation of the contributing terms in the vorticity in Eq. (1a) (see also Table 1). At the lower boundary the vertical velocity induced by the topography h_B is imposed as $\mathbf{v}\cdot\nabla h_B$, where h_B are the deviations from the average depth of the basin and $|\nabla h_B|$ is assumed to be of the order of the Rossby number to be consistent with the quasi-geostrophic approximation. We integrate equation (1) in a 250 × 250 km^2 region with horizontal resolution of 15.625 km. The vertical grid is composed

TABLE 1. List of symbols.

U_0	velocity scale = 10 cm s^{-1}
t_0	time scale = 11.5 (days^{-1}) = $(\beta_0 d)^{-1}$
d	horizontal scale = 50 km
f_0	Coriolis parameter at θ_0 = 29°N (7.07 × 10^{-5} s^{-1})
β_0	$\partial f/\partial y\|_{\theta=\theta_0}$ = 2 × 10^{-11} (ms)$^{-1}$
N_0^2	midthermocline Brunt–Väisälä frequency value
H	vertical scale = 700 m.
$N^2(z)$	climatological Brunt Väisälä profile
α	$=t_0U_0/d$ = 1.992
β	$=\beta_0 t_0 d$ = 1.
Γ^2	$=f_0^2d^2/(N_0^2H^2)$ = 1.015
σ	$=N_0^2/N^2(z)$, stability profile
ψ	geostrophic streamfunction or pressure
q	dynamical vorticity = $R + T$
R	relative vorticity $\nabla^2\psi$
T	thermal vorticity $\Gamma^2(\sigma\psi_z)_z$
$\dot{R}$	$=\partial_t\nabla^2\psi$
$\dot{T}$	$=\Gamma^2\partial_t(\sigma\psi_z)_z$
ΔF_R	$=-\alpha\mathbf{v}\cdot\nabla\nabla^2\psi$
ΔF_T	$=-\alpha\Gamma^2\mathbf{v}\cdot\nabla(\sigma\psi_z)_z$
ΔF_P	$=-\beta\psi_x$
F	Shapiro filter
K	kinetic energy = $(u^2+v^2)/2$
A	available gravitational energy = $\Gamma^2\sigma(\psi_z^2/2)$
$\dot{K}$	$=\partial_t K$
$\dot{A}$	$=\partial_t A$
ΔF_K	$=-\alpha\nabla\cdot(\mathbf{v}K)$
ΔF_π	$=-\nabla\cdot(\psi\nabla\psi_{zt}+\alpha\psi\mathbf{v}\cdot\nabla\nabla\psi-\beta\psi y\mathbf{v})$
δf_π	$=\sigma\Gamma^2\partial_z(\psi\psi_{zt}+\psi\mathbf{v}\cdot\nabla\psi_z)$
b	$=-\psi_z w$
ΔF_A	$=-\alpha\nabla\cdot(\mathbf{v}A)$

of six levels at depths of 100, 400, 700, 1400, 2400, and 3950 meters which were chosen to match the Soviet current meter mooring sensor depths at the first four levels. The model vertical grid scheme is explained in Miller et al. (1983). The average depth of the basin is 5300 m and the maximum topographic slope is 0.001 (m m^{-1}) both in the zonal and meridional directions.

At each interface of the model we have to assign regional values of $N^2(z)$, obtained by long term temporal and spatial averages. The averaged $N^2(z)$ profile is taken from the calculated values in the MODE-I region (MODE-I Atlas, 1977). The $N^2(z)$ profile linearly interpolated in a regular vertical grid is plotted in Fig. 2a. We calculate the vertical eigenfunctions $\phi_n(z)$ for this profile solving the eigenvalue problem

$$\Gamma^2(\sigma\phi_{nz})_z = -\lambda^2\phi_n$$

with $\phi_{nz} = 0$ at the top and bottom interfaces of the model. The first and second baroclinic eigenfunctions ($n = 1, 2$) are shown in Fig. 2b. The zero crossing of the first baroclinic mode is at 1200 m and the second baroclinic mode has two zero crossings at 325 and 2600 m. The internal Rossby radii are 44.07 and 19.26 km for the first and the second baroclinic modes respectively. The model computes the same eigenfunctions and eigenvalues but with six vertical levels. The first baroclinic mode is well reproduced by the model coarser grid and the first eigenvalue is 43.35 km. The shape of the second baroclinic mode is not impressive, but the eigenvalue is very close with a value of 20.27 km.

The model parameters are determined by the choice of $t_0 = (\beta_0 d)^{-1} = 11.5$ days, $U_0 = 10$ cm s^{-1}, $N_0^2 = 2.25 \times 10^{-5}$ sec^{-1}, $d = 50$ km, $\beta_0 = 2.10^{-11}$ (sec^{-1} m^{-1}) and they are also listed in Table 1. The POLYMODE SDE dataset used in this investigation consists of approximately 4000 XBT profiles from the surface to 800 m and of the Soviet-POLYMODE 19 current meter array. The XBTs covered an area of approximately 500 × 500 km^2 and the current meter arrays cover an area of approximately 300 × 300 km^2, as shown in Fig. 1. The current meter moorings were spaced 72.2 km apart. On each mooring the current meters were located at depths of 100, 400, 700 and 1400 meters. Here we will use only the information from the current meters at 700 and 1400 m since the data were analyzed in an early phase when no current meters at 100 and 400 were available. The XBT measurements considered are in the same area as the current meter moorings. The XBT and current meter datasets extend approximately from July 1977 to July 1978 (see Table 2). We will study only the data subset from Julian day 3350 to 3710 because of data sparsity during the very beginning and the end of the dataset. The detailed primary analysis of this dataset, called POLYMODE SDE Mark-2, is presented in Carter (1983) and Carter and Robinson (1986).

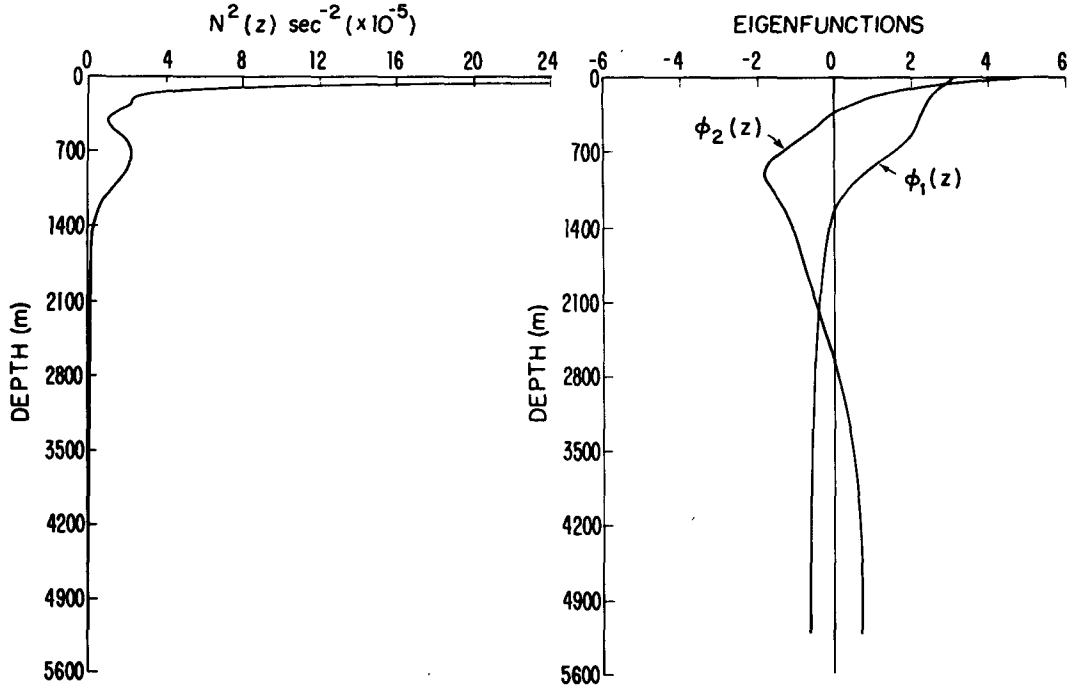

FIG. 2. (a) $N^2(z)$ profile for the MODE-I region. (b) First and second baroclinic dynamical eigenfunctions for the $N^2(z)$ profile of (a), in nondimensional units.

TABLE 2. Conversion table from Julian day to day/month/year.

Julian day	day/month/year
3350	25 Jul 1977
3420	3 Oct 1977
3450	2 Nov 1977
3560	20 Feb 1978
3580	12 Mar 1978
3630	1 May 1978
3660	31 Jul 1978
3710	19 Jul 1978

3. The streamfunction field: Analysis procedure

We describe the procedure of analysis of the XBT and current meter data which produce the streamfunction fields used to initialize and update the boundary conditions for the quasi-geostrophic model. We calculate geostrophic streamfunction from the dynamic height at 100 and 400 meters relative to 700 meters using the thermal wind relationship. The information from the current meters at 700 and 1400 meters is then used to generate four levels of absolute streamfunction at 100, 400, 700 and 1400 meters. We extend the pressure field down to the deeper levels (2400 and 3950 meters) using a projection on dynamical modes.

The XBT profiles were analyzed at each measurement site to produce dynamic height anomaly at 100 and 400 meters relative to the 700 meter level. This reference level was chosen because the current meter data were available at this depth, enabling us to obtain absolute streamfunction as explained here. The dynamic height anomaly, ΔD, between two pressure surfaces, p_1 and p_2, is written

$$\Delta D = \int_{p_1}^{p_2} \delta(p)dp \tag{2}$$

where

$$\delta = \frac{1}{\rho_{S,T}} - \frac{1}{\rho_{35,0}} \tag{3}$$

is the specific volume anomaly. The T–S diagram for the MODE region (MODE Atlas, 1977) was used to evaluate (3) using the algorithm written by Fofonoff and Millard (1983). The streamfunction $\psi(x, y, z, t)$ is related to the dynamic height anomaly by

$$\Delta\psi = \frac{\Delta D}{f_0} + F(p_1, p_2) \tag{4}$$

where f_0 is the Coriolis parameter listed in Table 1. The symbol Δ indicates the difference between the streamfunction at 100 or 400 meters and the reference field at 700 meters. The dynamic height has been objectively analyzed via a space–time anisotropic algorithm developed by Carter and Robinson (1986). The correlation function was calculated from the dataset itself assuming that the detrended statistics are homogeneous and stationary.

The current meters at the 700 and 1400 meter levels were analyzed via a vector objective analysis technique that is also described in the aforementioned paper. The interpolated u, v fields were used to find the geostrophic pressure distribution by solving the Helmholtz equation

$$\nabla^2\psi = v_x - u_y \tag{5}$$

at each level, using Neumann boundary conditions. The mooring measurements were not high quality because they used Savonius rotor current meters on surface-buoyed moorings, a system which is known to be accuracy deficient (Heinmiller, 1983; Polloni et al., 1981). The current meter speeds were too large by a factor 1.75 in magnitude, but the error in the direction of the velocities was negligible. The correction was made before performing the objective analysis. Carter (1983) and Carter and Robinson (1986) made a detailed study of the use of different statistical correlation functions for the objective analysis as applied to the current meter dataset. Here we use the empirical correlation function they calculated from the dataset itself and we apply it to the u, v velocity components separately. The objective analysis used a spatial window of 5 to 10 influential points and a temporal window of 5 days, except for sparse data periods.

The dynamic height is transformed to absolute streamfunction at 100 and 400 meters by adding the streamfunction calculated from the current meters at 700 meters. The function $F(p_1, p_2)$ is found by imposition of a zero long-term regional space and time average of the model density anomaly, i.e.,

$$\frac{1}{L^2T}\int_L\int_L\int_T \psi_z dtdxdy = \overline{\langle\psi_z\rangle} = 0 \tag{6}$$

where L is the length of each side (250 km), T is the time series length and the symbols $\langle\varphi\rangle$ and $\bar{\varphi}$ indicate space and time average of the φ field respectively. It follows immediately that $F(p_1, p_2) = \overline{\langle\Delta D\rangle}$. We also impose that $\langle\psi|_{z=700}\rangle = 0$ at each time since the streamfunction at all levels is always determined by less than a function of time. At the end of this procedure we obtain absolute streamfunction at 100, 400 and 700 meters.

The streamfunction at 1400 meters is still determined by less than a function of time, $c(t)$, since no temperature information is given at that level. We have to "extrapolate" the information from the upper levels. We fit the first baroclinic modal amplitude $\phi_1(z)$ shown in Fig. 2b to the density anomaly at the 250 and 550 m levels, which represent the intermediate levels between 100–400 and 400–700 meters. Thus we write

$$\psi_z|_{z=250} = (\phi_{1z}|_{z=250})\psi_1^{xbt}(x, y, t)$$
$$\psi_z|_{z=550} = (\phi_{1z}|_{z=550})\psi_1^{xbt}(x, y, t) \tag{7}$$

where ϕ_1^{xbt} indicates the first baroclinic modal amplitude deduced only from XBT data levels. Since we have only three absolute streamfunction levels from

the XBT data, as described, the second baroclinic mode is not resolved by the data and we neglect it. The first baroclinic streamfunction modal amplitude ψ_1^{xbt} is found via a least-squares fit by requiring that Eq. (7) holds. We write the streamfunction at level z_k in approximate form as

$$\psi(x, y, z_k, t) = \phi_0\psi_0(x, y, t) + \phi_1(z_k)\psi_1(x, y, t) \quad (8)$$

where the contribution from higher baroclinic modes is neglected. To find $c(t)$ we write the equality

$$\int_{1400}^{700} \psi_z dz = \psi|_{z=700} - \psi|_{z=1400}$$

$$= \psi_1^{xbt}(\phi_1|_{z=700} - \phi_1|_{z=1400}) \quad (9)$$

using (8); the space average of (9) gives

$$\langle\psi|_{z=1400}\rangle = c(t) = \langle\psi_1^{xbt}(x, y, t)\rangle(\phi_1|_{z=700} - \phi_1|_{z=1400})$$

and $c(t)$ is added to the streamfunction values obtained from (5) at 1400 meters.

We now have four levels of absolute streamfunction: we need to extrapolate the geostrophic pressure field to 2400 and 3950 meters. We have already found an estimate of the first baroclinic modal amplitude (ψ_1^{xbt}) from (7). Having two other independent measurements from the current meters at 700 and 1400 meters, we can estimate again the first baroclinic modal amplitude, this time called $\psi_1^{cm}(x, y, t)$, and the barotropic amplitude $\psi_0(x, y, t)$. We write a "best" estimate of $\psi_1 = (\psi_1^{xbt} + \psi_1^{cm})/2$ and we project down to the deep levels using (8). We believe that the information content or error level in the XBT and current meter measurements is comparable. There is no a priori reason to choose different "best" estimates: because of the different data sparsity in the XBT and current meter measurements, we feel that the average is a consistent, even though conservative, procedure. This procedure is applied to the entire 360 day data series; the streamfunction is also temporally smoothed by a Gaussian filter with an e-folding time of three days and a temporal window of ±6 days around the central day.

4. Events in the data series

Here we describe the qualitative features of the horizontally averaged kinetic energy density time series for the 360 days of the dataset at 100, 400, 700 and 1400 meters. The aim is to identify the characteristics of different periods and isolate particularly strong events in the time series.

The kinetic energy density integrated over 187.5 × 187.5 km^2 at the upper thermocline levels (100, 400 and 700 m) is shown in Fig. 3a. It is possible to note high energy peaks in the first 100 and last 150 days of the data series and a more quiescent period of 100 days in the middle. The temporal width of the peaks is approximately 30–40 days from one relative minimum to the next, but a 20 day variability is also present. The mean kinetic energy densities at 100, 400 and 700 meters are 90, 63 and 40 cm^2 s^{-2}, respectively. These values, although referred to as the total kinetic energy density, are intermediate between the MODE and the POLYMODE LDE experiment eddy kinetic energies at these levels (Owens et al., 1982). They are less intense at the surface than the LDE eddy kinetic energies but more intense that the MODE-I regional values. The kinetic energy standard deviations are 44, 33, 21, cm^2 s^{-2} at 100, 400, 700 meters respectively.

The deep level kinetic energy time series is presented in Fig. 3b; it shows a short time scale variability superimposed on an apparently quadratic trend. The short time scale variability has approximately the same time scale as the upper thermocline levels (30–40 days) with an enhanced 20-day variability. Although all the major peaks have some correlation with the peaks in the upper thermocline levels, there are no "outstanding" peaks in this time series. However, the first and last fifty days appear to be more energetic than the middle periods also at this level. The mean kinetic energy at this level is 18 cm^2 s^{-2} and the standard deviation is 8 cm^2 s^{-2}.

The horizontal and vertical integral of the kinetic energy in the barotropic and first baroclinic modes E_i, $i = 0, 1$ is defined as

$$E_i = \frac{1}{H}\int_{-H}^{0} \frac{\langle(\psi_{ix}^2 + \psi_{iy}^2)\rangle}{2}\phi_i^2(z)dz$$

and is shown in Fig. 4. The mean kinetic energy in the barotropic, E_0, and first baroclinic mode, E_1, are 18 and 8.7 cm^2 s^{-2}, and the standard deviations are 7.3 and 3.3 cm^2 s^{-2}, respectively. Thus, the ratio between the time averaged kinetic energy of the barotropic and first baroclinic mode is approximately 2 and the variance in the barotropic mode is a factor of 5 larger.

The trend in the barotropic modal energy time series is similar to the 1400 meter total kinetic energy time series, suggesting that a strong correlation exists between the two of them; superimposed on this trend, is a time scale variability shorter than the baroclinic one. The first baroclinic mode kinetic energy shows very regular peaks, especially during the first 150 days; the only outstanding peak is at the end of the data series around 3650. The barotropic time series has an enhanced 20-day time scale variability; the impression is that if the quadratic trend would have been subtracted, a regular sequence of peaks would have emerged. The peaks in the kinetic energy time series at the upper thermocline levels coincide with some of the highest peaks in the barotropic and/or baroclinic kinetic energy content, as described here.

In this paper we concentrate on the dynamical interpretation of the processes occurring during the three major kinetic energy peaks at the upper thermocline levels. From Fig. 3a we can distinguish three different periods of high energy peaks:

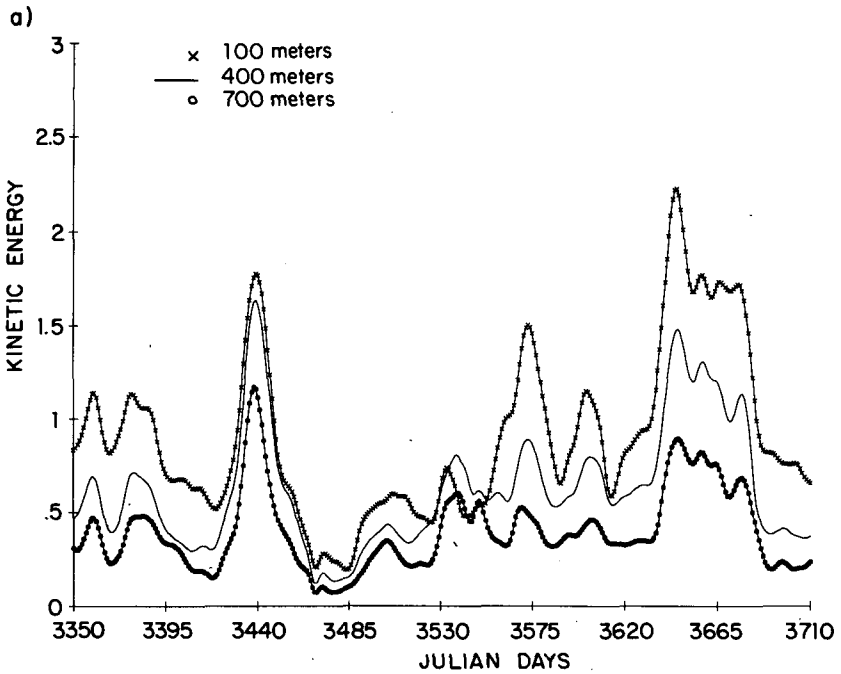

FIG. 3a. Averaged kinetic energy density time series at 100, 400, and 700 meters. The domain of integration is 187 × 187 km^2. Multiply by 100 to obtain dimensional values in units of centimeter squared per second squared.

1) Period 1, starting at Julian day 3420 and ending at Julian day 3460. It is the highest peak (deviation from the mean) at 700 and 400 m and the second highest at 100 m. At the same time the 1400 m time series also shows a noticeable peak. This is the period with higher coherence in the kinetic energy fluctuations between the upper and lower thermocline levels.

2) Period 2, starting at Julian day 3550 and ending

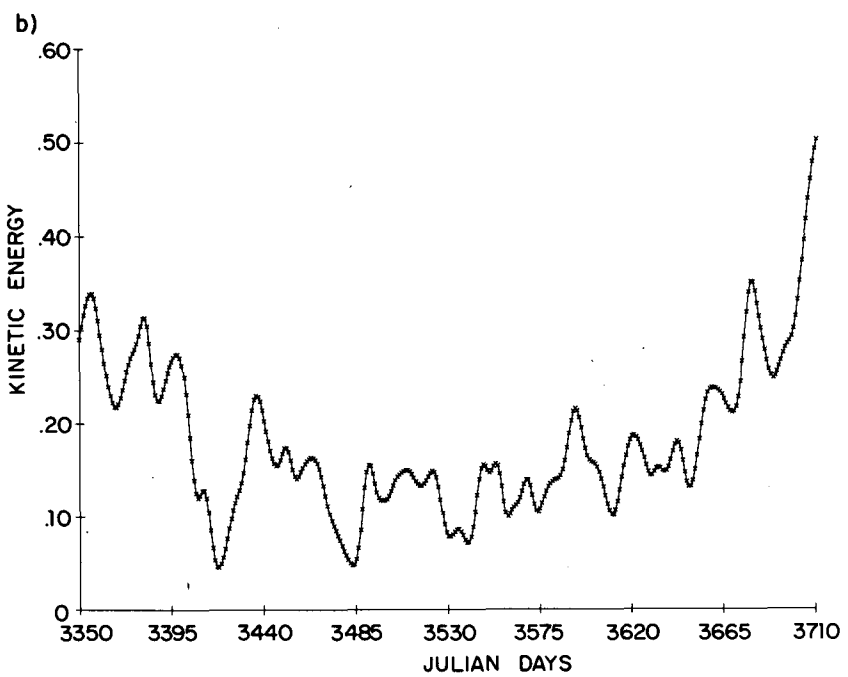

FIG. 3b. As in Fig. 3a, but at 1400 m.

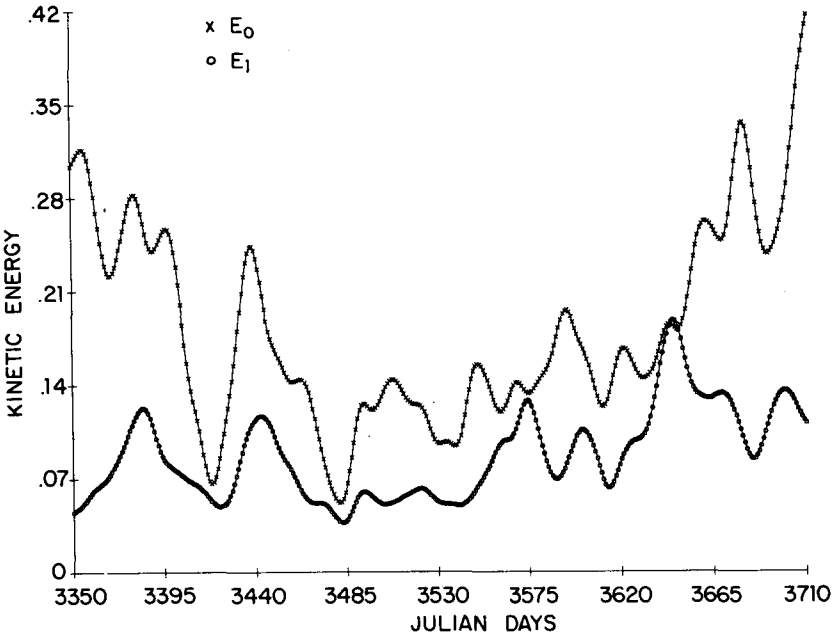

FIG. 4. Barotropic (E_0) and first baroclinic (E_1) kinetic energy density time series. See text for definition of E_0, E_1.

at Julian day 3590. The energy peak at 100 and 400 m are the third highest discounting the weaker signal at 700 m. At 1400 m the kinetic energy time series shows a peak starting earlier (3540) and decreasing in amplitude during the period of maximum kinetic energy at 100, 400 and 700 m. No clear relationship exists between the two different peak periods at the upper and lower thermocline levels.

3) Period 3, starting at Julian day 3630 and ending at 3690. It is the highest energy peak found at 100 meters and the second highest at 700 and 400 meters. The 1400 m time series does not show any outstanding peak analogous to Period 2 before. This upper thermocline peak has the fastest growth rate in the time series and at 100 m the kinetic energy does not decay as rapidly as during the other periods as it reaches an absolute maximum and it stays on a high energy plateau for 30 days.

In the baroclinic and barotropic kinetic energy time series, Period 1 is also different from periods 2 and 3. Period 1 coincides with a relative maximum in both barotropic and baroclinic kinetic energy. The barotropic peak is one standard deviation away from the mean. Periods 2 and 3 coincide only with a relative maximum in the baroclinic energy; the energy in the barotropic mode starts to grow at the end of the two periods and reaches a relative maximum in the next 20 days. Notice that during periods 2 and 3 the baroclinic and barotropic energies become comparable.

The streamfunction has been sampled at three levels (100, 700, 1400 m) during the three different periods and is shown in Fig. 5. During Period 1, (Fig. 5a) the pressure pattern shows a weak zonal jet entering the region; 20 days later the velocities along the southern border of the jet are at least doubled and a small but strong cyclonic closed circulation is formed in the whole region. The current meters superimposed on the 700 m pressure pattern show the local growth of energy in the jet and in the cyclone. At the same time a strong meandering jet is formed at the 1400 meter level. The jet is part of a larger eddylike feature which is not resolved by our domain but evident in the streamfunction maps on a larger domain 500 × 500 km^2 (Bogden, 1983; Carton and McGillicuddy, 1985).

The beginning of Period 2 shows instead a meridionally oriented jet separating two eddy centers that are strongly intensified at the surface (Fig. 5b); the jet meanders and strengthens during the following twenty days. At 1400 m the flow pattern has no immediate visual similarities with the upper thermocline flow and only 20 days later the pressure pattern acquired more vertical coherence. The western jet appears to meander and intensify also at 1400 m. There is a tendency in the pressure pattern to form a closed cyclonic circulation at the border of the jet. At day 3585 (not shown) a closed cyclonic circulation appears in the domain, first at 1400 m and then at the upper levels, but in the latter case the jet is already out of the domain.

The Period 3 pressure pattern is shown in Fig. 5c. Once again, the domain is occupied by two anticyclonic centers enveloped in a larger meridional jetlike circulation, strongly intensified in the upper thermocline

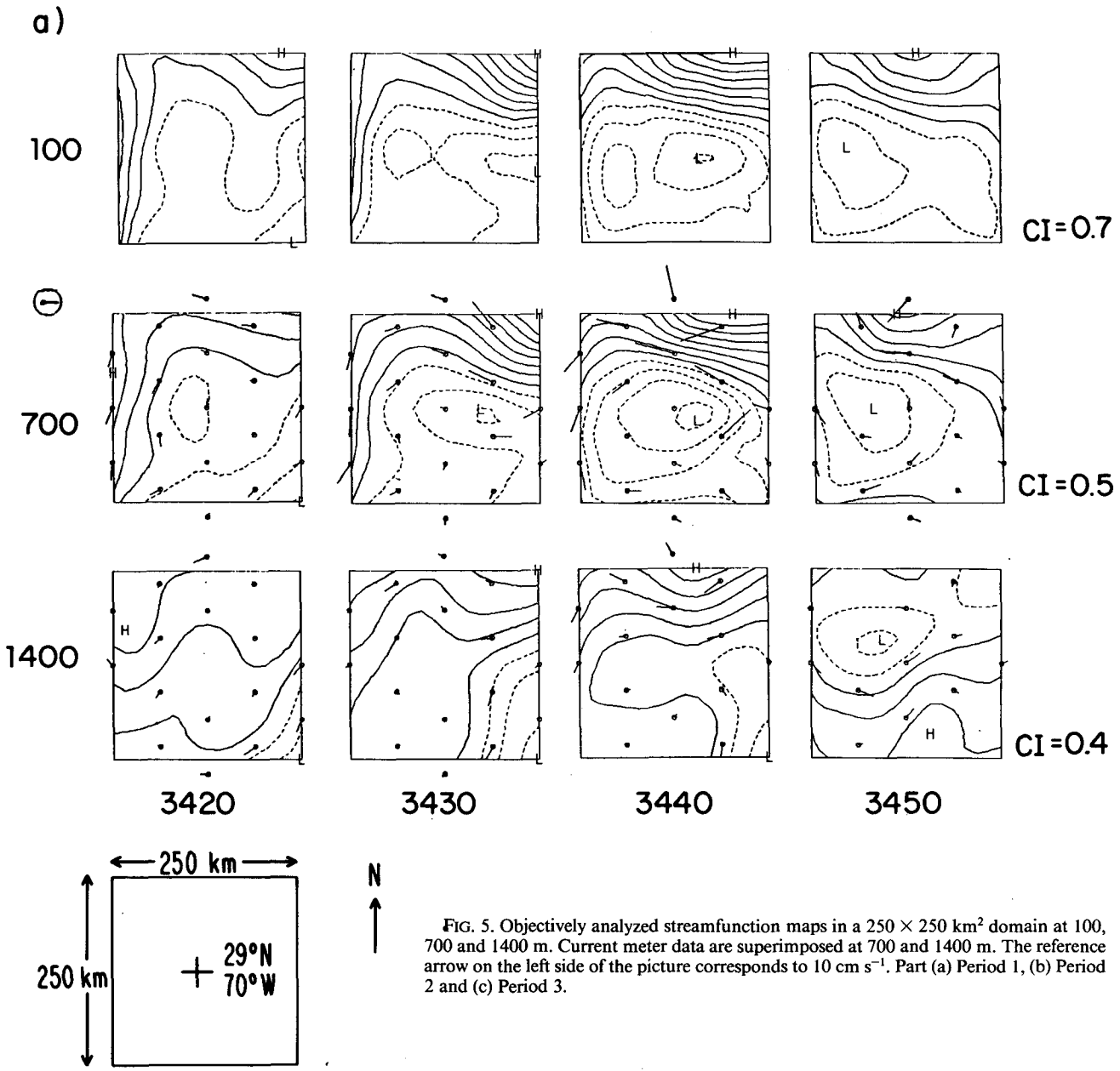

FIG. 5. Objectively analyzed streamfunction maps in a 250 × 250 km^2 domain at 100, 700 and 1400 m. Current meter data are superimposed at 700 and 1400 m. The reference arrow on the left side of the picture corresponds to 10 cm s^{-1}. Part (a) Period 1, (b) Period 2 and (c) Period 3.

levels. The jet around the northern anticyclonic eddy strengthens very rapidly and a cyclonic closed circulation forms at its border. Similarly to Period 2, the vertical coherence of the pressure patterns is very low. At 1400 m only a dipolar structure is present at day 3630 which strengthens at 3640. Between Julian days 3640 and 3650 a zonally elongated jet enters the domain from the northeastern side. It merges with the anticyclonic circulation at the western border and now only a very small cyclone is evident at the center of the domain. After day 3650 the small cyclone moves southward at all levels and at 1400 m a strong jet is formed at the northern edge of the domain. The strengthening of the jet and the development of a closed cyclonic circulation at its border is also seen in the LDE area 20–30 days later and the visual similarity of the pressure pattern evolution is evident. This thermocline jet is described by McWilliams (1983a) and Hua et al. (1986) as one of the most intense features of the LDE dataset. During the following 30 days (not shown) the domain is invaded by another very intense anticyclonic eddy. This explains why in the kinetic en-

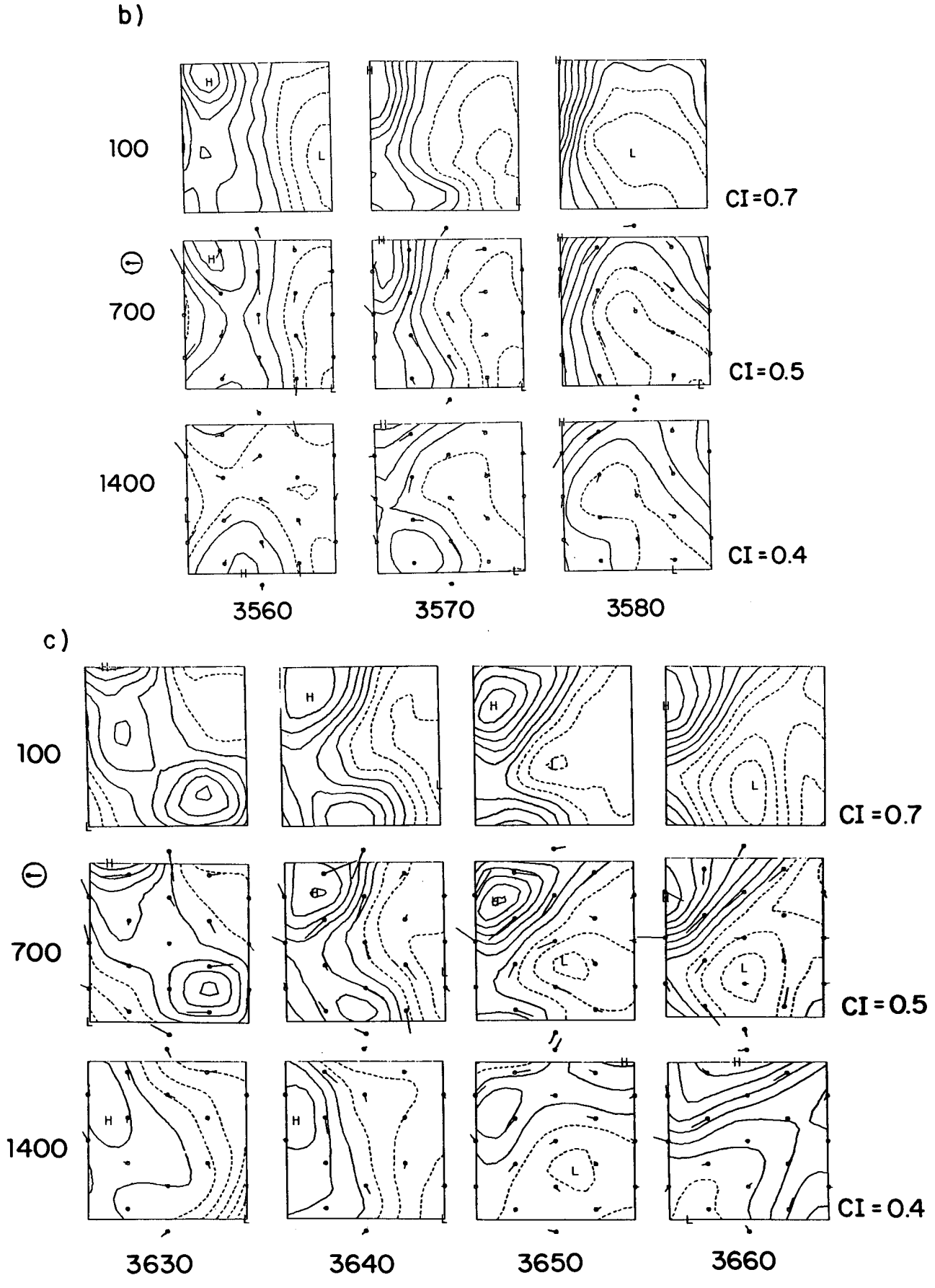

FIG. 5. (*Continued*)

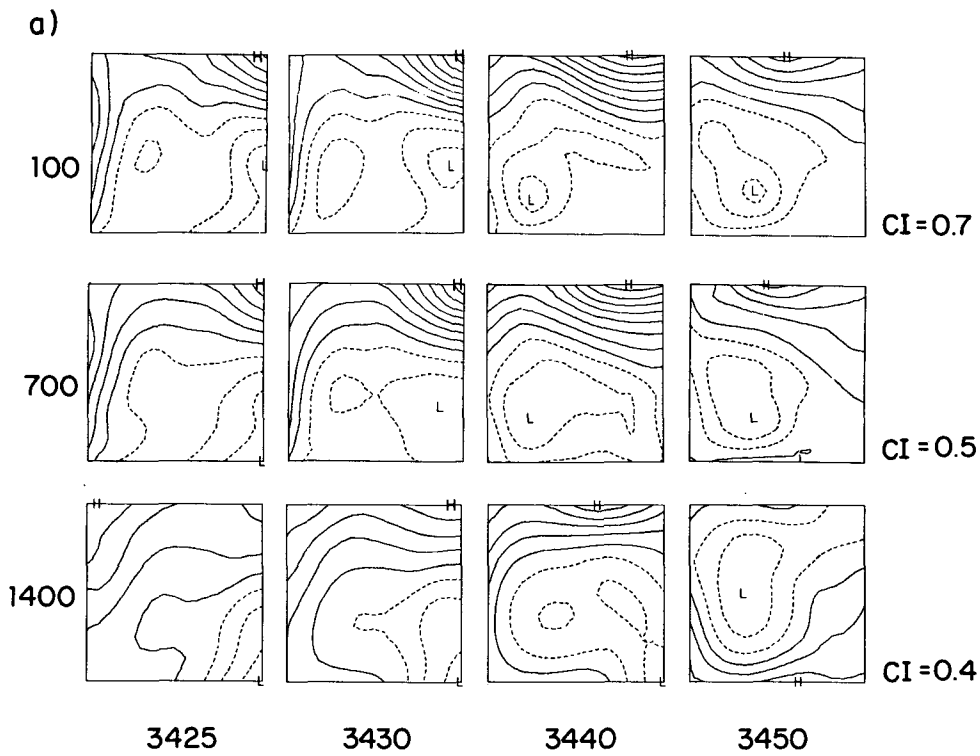

FIG. 6. Streamfunction ψ at different time and levels for the forecast experiments: (a) period 1, (b) period 2, (c) period 3.

ergy time series of Fig. 3a the energy does not decay rapidly in the domain after the jet has left the region.

In conclusion, the three highest peaks in the data series coincide with jet amplification, meandering and eddy formation processes in the domain. The jet has a strong signature at all the thermocline levels down to 1400 m. Periods 2 and 3 seem to be distinct from Period 1 because the upper thermocline levels (100, 400, 700 m) are less coherent with respect to the 1400 m kinetic energy peaks, baroclinic and barotropic energy growth in the domain are not simultaneous and the flow is meridionally elongated.

5. Dynamical interpolation

Here we illustrate the results of the dynamical assimilation of the data in the quasi-geostrophic open ocean model for the three periods described in the preceding section. To apply EVA we need to "filter" the data in order to evaluate the high order derivatives. The quasi-geostrophically adjusted fields contain the same features present in the data and they are consistent with the dynamical vorticity balance described by (1). The methodology of the approach for application of EVA to real ocean dynamics is illustrated in Pinardi and Robinson (1986) and the strategy of dynamical interpolation of real mesoscale data in the ocean is illustrated in Robinson et al. (1986), hereafter called RCPM. The forecast experiments are chosen to be 30 days long for Period 1 (3420–3450) and Period 3 (3630–3660), but only 20 days for Period 2 (3560–3580). The very poor data distribution day 3550 did not allow the initialization of the model at 3550. Here we integrate the model forward from an initial streamfunction, ψ, and an initial potential vorticity, q, updating the boundary condition on ψ and q at every time step. The time step is 3 hours and a simple linear interpolation in time is used between "data days." An eighth-order Shapiro filter is applied once every time step on the vorticity. Experiments also were performed with second- and fourth-order Shapiro filters. Since the duration of the forecast experiments was relatively short and the initial vorticity fields were not very noisy (due to the high data quality), the use of a higher order filter was preferable due to its steeper response curve in wavenumber space.

In Fig. 6 the results of the three forecast experiments are presented for the same levels as the data maps shown in Fig. 5. For each period examined, a set of forecast experiments were carried out with and without bottom topography. There is little visual difference in the results; Fig. 6 is for flat bottom. The Period 1 forecast (Fig. 6a) shows that the model reproduces the strengthening of the jet and the development of the closed cyclonic circulation in the center of the domain but the cyclone is weaker and its center is more shifted toward the western side of the domain. It is interesting to note that the cyclonic circulation has a very small

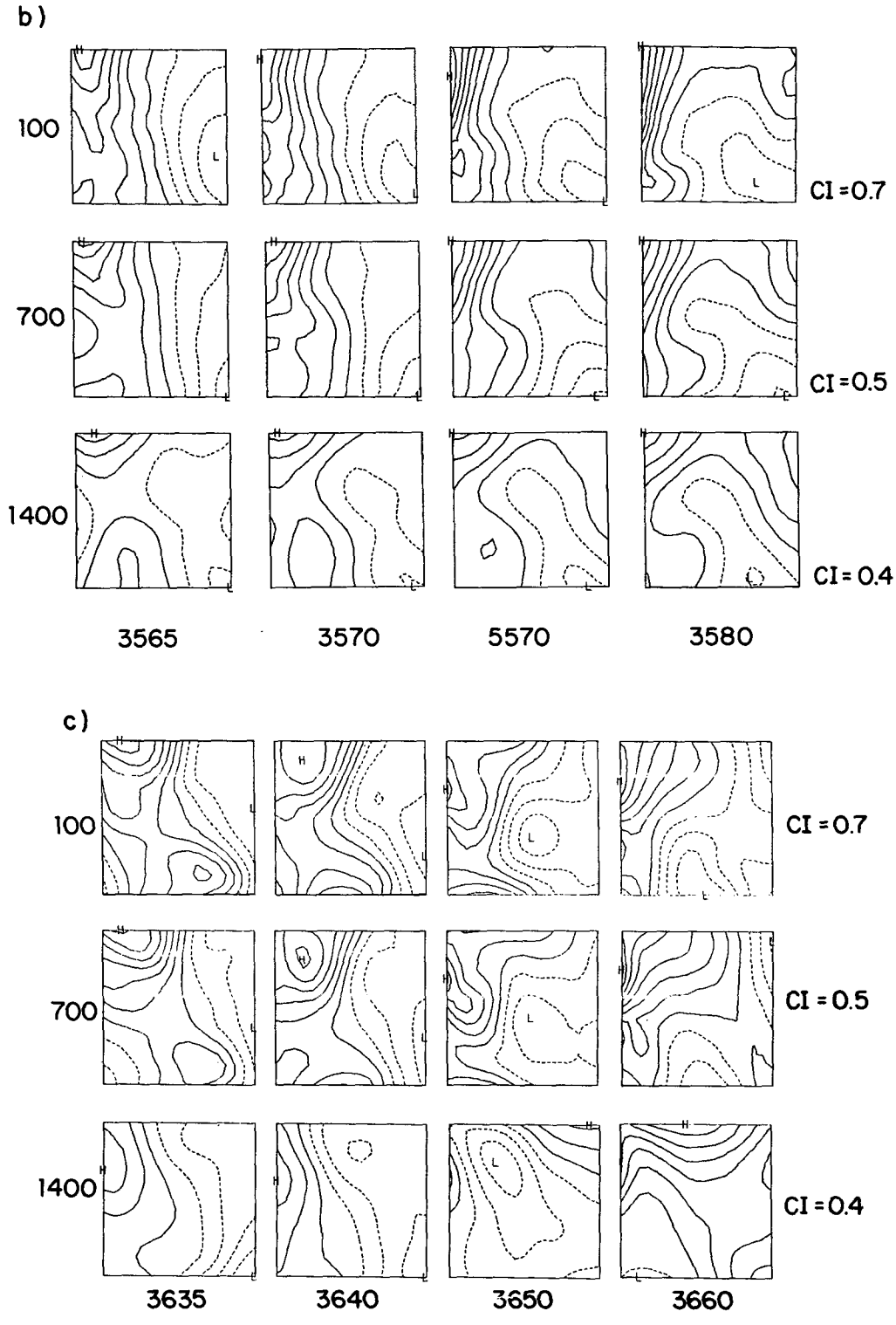

FIG. 6. (*Continued*)

size (50–60 km radius); it shows a very strong pressure signature first at the upper levels and later at deeper levels. The jet at 1400 m is well formed by the model although it is slightly stronger than in the observed objectively analyzed fields.

The model calculates statistical diagnostic values for

the root-mean-square (rms) difference fields and the absolute correlation values (cor), defined respectively as

$$\text{rms} = \left[\frac{\langle(\psi_f - \psi_r)^2\rangle}{\langle\psi_r^2\rangle}\right]^{1/2}$$

$$\text{cor} = \frac{\langle(\psi_f - \langle\psi_f\rangle)\rangle\langle(\psi_r - \langle\psi_r\rangle)\rangle}{[\langle(\psi_f - \langle\psi_f\rangle)^2\rangle\langle(\psi_r - \langle\psi_r\rangle)^2\rangle]^{1/2}}$$

where ψ_r and ψ_f are the objectively analyzed and the forecast fields respectively. For the flat bottom case the rms difference is 25% averaged on the 30 days of the forecast at 100, 400, 700 m and 70% at 1400 m. The absolute correlation is, on average, 0.97 for the 100, 400 and 700 m levels and 0.85 at 1400 m. In this period, the introduction of bottom topography decreases the rms difference errors by 10% at the three upper thermocline levels (100, 400, 700) indicating that some interaction of the baroclinic waves with the topography is present.

It is informative to study the behavior of the system in the neighboring physical space of model parameters. The Γ^2, α, β in (1) measure the relative importance of: thermal to relative vorticity effects, local time changes to advective, and nonlinear versus planetary vorticity effects. To understand the essential physics of the processes involved, we carried out a series of parameter sensitivity experiments. With $\alpha = 0$ the forecast was very poor and no jet strengthening and cyclone formation occurred in the domain. Increasing Γ^2 by a factor of 5, makes a stronger jet and a more intense cyclonic circulation. This result suggests that the process is connected with a baroclinic conversion of energy in the water column. The XBT data distribution between Julian day 3420 and 3430 is very poor: the initialization fields at day 3420 are then smoothed between the data rich days which are concentrated in the time windows 3410–3420 and 3430–3440. The result is that the initial condition at 3420 is due only to the objective analysis time interpolation and this is significant because the forecast experiment depends strongly on the initial condition. We have initialized a forecast at Julian day 3430 where the XBT data coverage is very good: the result is that the cyclone is now as strong as in the objective analysis data and the jet has a more realistic shape. However, the strong internal dynamical evolution of the flow field (jet intensification and cyclonic eddy formation at its border) at all thermocline levels is correctly captured by the model in the 30-day forecast. Thus we will use the 30-day forecast with topography for EVA, allowing us to evaluate energy fluxes for the duration of the process.

The second forecast experiment is shown in Fig. 6b for Period 2. The model reproduces the meridional jet strengthening and meandering but with a visible greater richness of wavelengths along the jet, perhaps not resolved by the XBT spatial resolution. The jet is also well formed at 1400 m although it is strongly surface intensified. The rms difference error is 25% at the three upper levels and 30% at 1400 m; the absolute correlation is 0.95 at all levels. In this period, the introduction of the topography increases the accuracy of the forecast experiment by only a few percent. The EVA will be applied to the topographic forecast experiment.

The third forecast experiment is shown in Fig. 6c for Period 3. The forecast is good at 3640 and the jet is formed at all levels. Already a small closed cyclone forms at the border of the jet; it will intensify later in the forecast and finally it will propagate southward out of the domain. The data at 3650 (Fig. 5c) show the small cyclone moving southward very rapidly at 1400 m; the speed of propagation of this feature is underestimated by the forecast. A jetlike structure enters the domain at 1400 m from the northeast 20 days later than at the upper thermocline levels. It will line up with the upper thermocline jet, intensifying and meandering also at 1400 m and deeper levels. The vertical phase tilt of this feature is very steep and consistent with a high first baroclinic kinetic energy peak in this period as seen in the data of Fig. 4. At 3650 the jet is well formed but the closed anticyclonic eddy at the northwest border is propagating too fast due to inaccurate boundary conditions. Between Julian day 3650 and 3660 there are in fact almost no XBT data and the objective analysis is propagating the information from 3660 toward the boundaries of the domain too quickly. Relatively poor data quality is influencing the forecast from day 3645 until 3660, but still the strong internal dynamical evolution and strengthening of the jet is reproduced by the model.

The accuracy of the forecast without topography is higher in the sense that the rms was decreased by 5–10% at the three upper thermocline levels. This could be due to the absence of XBT data between day 3650 and 3660 which gives a very bad estimate of ψ_1^{xbt} (see section 2) and thus of the temperature estimate at 1400 meters. The average rms error is 35% at the three upper levels and 60% at 1400 m; the absolute correlation is 0.95 at 100, 400 and 700 and 0.75 at 1400 m. A parameter sensitivity experiment with $\Gamma^2 = 5$ shows the formation of a stronger jet and a much higher kinetic energy peak. Starting at day 3640 the forecast does not do much better since this time the poor data quality is not in the initial condition but in the boundary conditions which affect the twenty and thirty day forecasts the same way. Thus, for this period, EVA will be applied to the thirty day forecast without topography.

6. EVA Energy and Vorticity Analysis: Jet and cyclone formation processes

In this section we present the study via EVA of the mesoscale processes which occurred during the three forecast experiments described in section 5. The results indicate that, at least for these three events, the source

of kinetic energy for the intensification of the baroclinic jet is local and it is due to baroclinic conversion of available gravitational energy (A) into kinetic energy (K). Furthermore, there is a large export of kinetic energy via horizontal pressure work energy divergences and enhanced vertical energy exchange among the various levels. The equations for EVA are presented in Pinardi and Robinson (1986, hereafter referred to as PR). We will present here only a brief description of the formalism. The kinetic and available gravitational energy equations for the geostrophic streamfunction field are

$$\partial_t K = -\alpha\nabla\cdot(\mathbf{v}K) + \nabla\cdot(\psi\nabla\psi_t + \alpha\psi\mathbf{v}\cdot\nabla\nabla\psi + \beta\psi\mathbf{v}y) + \partial_z(\Gamma^2\sigma\psi\psi_{zt} + \Gamma^2\alpha\sigma\psi\mathbf{v}\cdot\nabla\psi_z) - \psi_z w + D \quad (10a)$$

$$\dot{K} = \Delta F_K + \Delta F_\pi{}^t + \Delta F_\pi{}^a + \Delta F_\pi{}^\beta + \delta f_\pi{}^t + \delta f_\pi{}^a - b + D \quad (10b)$$

$$\partial_t A = -\alpha\nabla\cdot(\mathbf{v}A) + \psi_z w \quad (11a)$$

$$\dot{A} = \Delta F_A + b \quad (11b)$$

where $A = \Gamma^2\sigma(\delta^2/2)$, $K = (u^2 + v^2)/2$ and $\psi_z = \delta$ is the model density anomaly; D corresponds to the dissipation in the model, parameterized by the Shapiro filter on the total vorticity. Also, symbolically, $\Delta F_\pi = \Delta F_\pi{}^t + \Delta F_\pi{}^a + \Delta F_\pi{}^\beta$ and $\delta f_\pi = \delta f_\pi{}^t + \delta f_\pi{}^a$. The (a) versions are the explicit form of the energy flux divergences in terms of the geostrophic pressure field ψ and the (b) versions are the symbolic representations of the contributing terms (see Table 1).

The methodology of studying local energy and vorticity balances consists in mapping the various divergences in (10) and (11) together with the time series for their space averaged values. Finally, an energy diagram is computed for space–time averaged values of the contributing terms in (10) and (11), showing the net energy transport or conversion signature of each event. As shown in PR the signature of barotropic-baroclinic local instability is seen in the divergence maps as growth of asymmetric patterns (uneven spacing and unequal amplitudes of the highs and lows) and the positive (negative) definiteness of the divergences i.e., absolute value of the highs larger (smaller) than the lows. In particular, for the Eady baroclinic instability case (linear shear and constant stratification), PR shows that asymmetries grow in the b, δf_π, ΔF_π, ΔF_A terms such that b is negative definite, ΔF_A positive definite. These latter two terms are the most important signature of the process of local energy conversion in the Eady waves; furthermore, b has its strongest signature in the middle of the fluid column. Thus in a baroclinic amplification process it could be expected that the maximum of the baroclinic conversion occurs at intermediate and deep levels. PR shows that, in the pure baroclinic Eady wave case, both ΔF_π (negative definite) and δf_π (positive definite), play an important role in redistributing the energy horizontally and vertically in the open domain. As to be expected, these signatures are modified in the fully nonlinear processes explored here. However the competitive contributions of δf_π, b, ΔF_A, relative to ΔF_K, ΔF_π, still identify the importance of baroclinic conversion versus the horizontal flux divergences which represent the barotropic eddy energy sources in this formalism.

In the following we will describe EVA applied to periods 1 and 3 and then to period 2 because of the similarities between the processes in the different periods. The maps of the K and A energy balance terms have been stripped of the outer two gridpoints on each boundary so as to eliminate any possible effects from imposed boundary values, i.e., the forecast domain is 250×250 km^2 and the EVA domain is 187.5×187.5 km^2. Moreover, we will show primarily maps of the local balances at 1400 meters: the balances at 700 meters are similar but at smaller amplitudes. Furthermore, because of the level representation in vertical and the customary weighting of the ψ_z fields in (10) and (11) ($\psi_z{}^k = 0.5(\psi_z{}^{j-1} + \psi_z{}^j)$ with $k = 1, \cdots 6$ levels and $j = 0, \cdots, 6$ interfaces), the A and K balances at 1400 m physically represent the lower thermocline layer, from 900 m down to 1900 m.

a. Period 1 EVA

The vorticity balances are shown in Fig. 7 for the model level 4 (1400 m). The relative and thermal vorticity divergences are comparable and ΔF_R is at smaller scales than ΔF_T. This is true at all levels: ΔF_R shows a small scale wavelike pattern along the jet which strengthens between day 3430–3440. At level 3 and 4 ΔF_R and ΔF_T are comparable, whereas at the model levels 1 and 2 (100 and 400 m), ΔF_R is dominant locally in the absolute value of the highs and lows. The filter F is unimportant numerically except at level 1 and 2 around day 3430. The vorticity dynamics indicates the presence of wave propagation along the jet region which is shown by the meandering of the jet. Furthermore, it shows different dynamical balances in the upper and lower thermocline levels: the former are dominated by the relative vorticity terms and the latter by an equal contribution from all terms. The thermal ($\dot{T}$ and ΔF_T) and relative ($\dot{R}$ and ΔF_R) vorticity terms seem to balance between themselves separately since their spatial scales are different although there is a local phase lock between ΔF_R and ΔF_T.

Figure 8a shows the kinetic energy balances for level 4. Before day 3434 all the divergences have small amplitude and therefore they are not shown. The balance in the jet region is among ΔF_K, ΔF_π and δf_π, at level 4 and it is simply between ΔF_K and ΔF_π at levels 1, 2, 3. The components of δf_π, ($\delta f_\pi{}^t$, $\delta f_\pi{}^a$), are very large at levels 3 and 4 and before day 3434 they balance to give almost zero total δf_π. At Julian day 3434 the pattern changes dramatically. Level 4 starts to show a major contribution in the jet region from $-b$, and δf_π exports energy vertically in the same area where prior to this

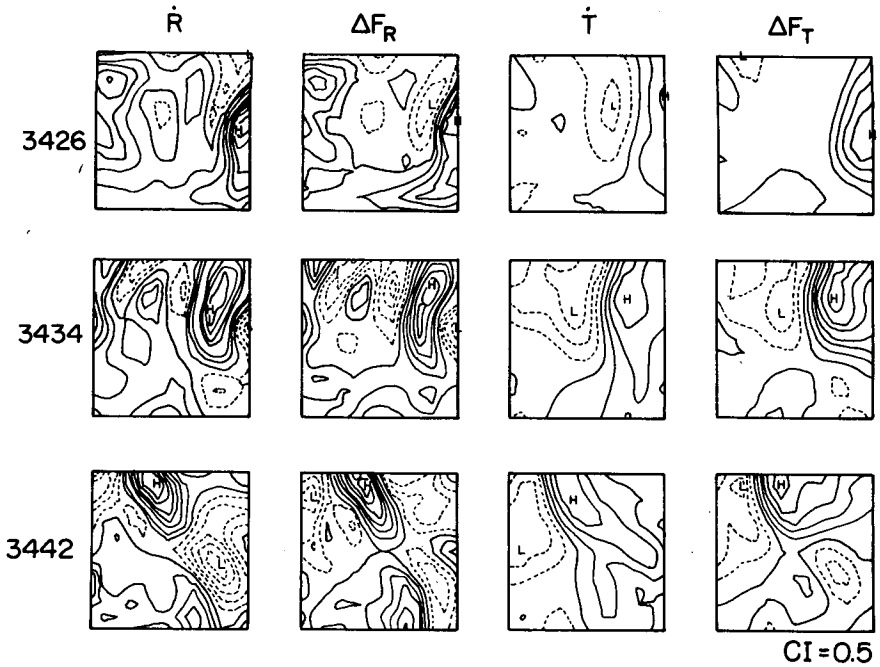

FIG. 7. Instantaneous maps of the vorticity terms at 1400 m in Eq. (1) for the forecast experiment of period 1.

time it was small but importing. In the jet region, ΔF_π and ΔF_K are positive definite; in the region southeast of the jet a dipolar structure (a high/low extreme pair) in δf_π and ΔF_π is present. At the same time, in the area of the jet, levels 2, 3 start to import energy via δf_π which is balanced by a negative ΔF_π; ΔF_K is also importing energy but at a slightly lower rate than before day 3434. Although not numerically significant in the $\dot{K}$ balance, $-b$ becomes positive in this area. A few days later (day 3442 in Fig. 8a) the pattern has changed radically again: all the divergence terms show a smaller scale wavelike pattern evident also at the other levels. The dipolar structure in the region southeast of the jet has changed, becoming a larger positive (negative) definite signal in ΔF_π (δf_π) and it is bottom intensified since its signature is numerically important at the deep levels 4, 5 and 6.

The $\dot{A}$ balance (Fig. 8b) also shows the dramatic changes in the balance which were evident in Fig. 8a. In this equation b is important at all levels and negative definite in the area of the jet starting from Julian day 3434; ΔF_A energizes the region, A increases and is converted to K via b. At level 3 ΔF_A shows the growth of small scale disturbances along the jet. The temporal growth of b shows that its maximum negative value grows first at 1400 m and then in the adjacent levels. In summary, in the $\dot{K}$ balance there are signatures of meandering and translation of the jet. While this is happening a burst of baroclinic instability occurs in the jet at the deep levels and energy is exported vertically from the 1400 and 2400 m levels into the upper thermocline levels. The process has a clear signature of energy transport/conversion typical of baroclinic instability in the $\dot{A}$ balance; in the $\dot{K}$ balance the process is impure since ΔF_K, ΔF_π are as important as the baroclinic terms and they import energy locally. Also, at 1400 meters δf_π^t (δf_π^a) is positive (negative) definite, consistent with normal mode baroclinic instability processes (see PR).

The formation and strengthening of the cyclonic eddy in the domain is fundamentally connected with the process of strengthening of the jet. The meandering of the jet is related to the short wavelike disturbances evident in the divergence terms as multipolar structures propagating along the jet during the intensification process. The waves have an important energetic signature at all levels before 3434; afterwards they develop very short meridional and zonal wavelength along the border of the jet. The cyclone development and steepening of a frontal zone is a process reminiscent of the local growth of baroclinic waves along inhomogeneous sheared flows. The mean flow is provided in this case by the border of a big eddy structure. To show the amplification of the wave on the border of the larger eddy not contained in our domain, we have taken differences between the streamfunction at the initial time and the forecasted ψ at later times. Figure 9a shows the difference fields. It is evident that the dipolar structure with the low pressure signature, corresponding to the cyclonic circulation, intensifies between days 3430–3440 inside the domain producing the strengthening of the jet and of the cyclone. Figure 9b shows the difference maps between the time averaged stream func-

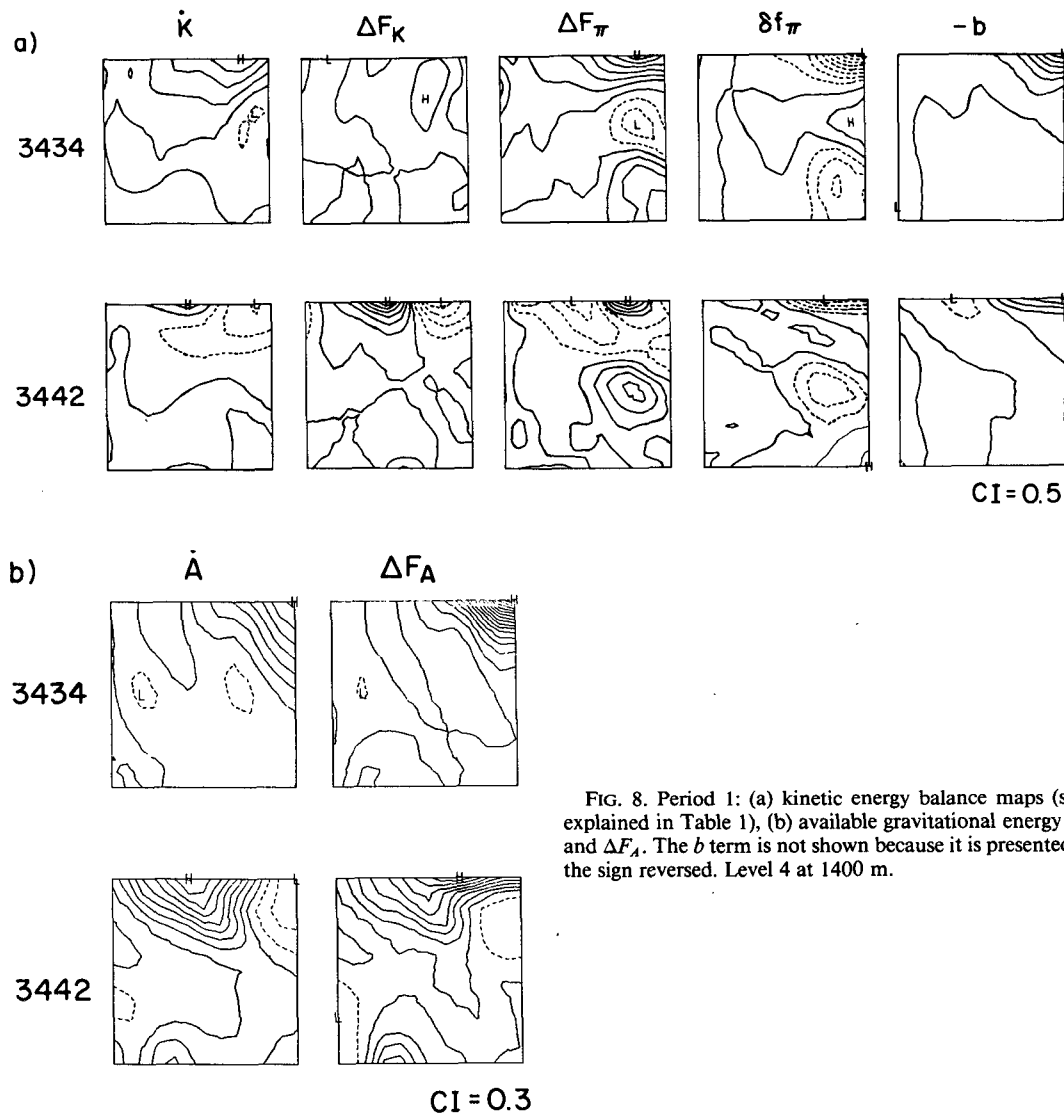

FIG. 8. Period 1: (a) kinetic energy balance maps (symbols are explained in Table 1), (b) available gravitational energy maps for A and ΔF_A. The b term is not shown because it is presented in (a) with the sign reversed. Level 4 at 1400 m.

tion $\overline{\psi(x, y, z, t)}$, and the instantaneous forecast ψ fields. We interpret this pattern as the indication that "perturbations" are growing on the "average" state predicted by the model. Again the dipolar structure (high pressure in the jet region and low pressure in the cyclone position) intensifies and does not seem to have any relevant velocity of translation with respect to the "average" flow between day 3430–3440. The local extraction process is accomplished in an effective way if the waves have almost zero group velocities with respect to the mean flow they grow on; this seems to be the case in our example since the $\Delta F_\pi{}^t$ and $\Delta F_\pi{}^\beta$ (Rossby wavelike radiative fluxes, see PR) are negligible in the balance until 3440. These behaviors support the interpretation of the almost stationary pattern in Fig. 9b before day 3440. After the baroclinic conversion has occurred there are signals of prominent translation of the jet and of the cyclone out of the region. At the very deep levels, after 3440, the balance is in fact dominated by $\Delta F_\pi{}^t$ and δf_π terms while the pressure field is dominated by the cyclone which moves out of the domain in the northwest direction following the border of the jet.

In Fig. 10 the time series of the space averaged values for the vorticity and energy balances are shown for the 1400 m level. The balance in the vorticity equation (Fig. 10a) is between $\langle \dot{R} - \Delta F_R \rangle$ and $\langle \dot{T} - \Delta F_T \rangle$ with no contribution from $\langle \Delta F_P \rangle$ until 3440 at which time the latter starts to grow. Also at 700 meters $\langle \dot{R} - \Delta F_R \rangle$ and $\langle \dot{T} - \Delta F_T \rangle$ tend to balance until day 3440 after which $\langle \Delta F_P \rangle$ balances $\langle \dot{R} - \Delta F_R \rangle$. The $\langle \Delta F_P \rangle$ is important at all the other upper thermocline levels (100, 400 m) and it balances $\langle \dot{T} - \Delta F_T \rangle$: very different dynamical balances occur in the water column. At 100, 400 and 700 m the integrated vorticity balances show a shorter time scale of variability with respect to 1400

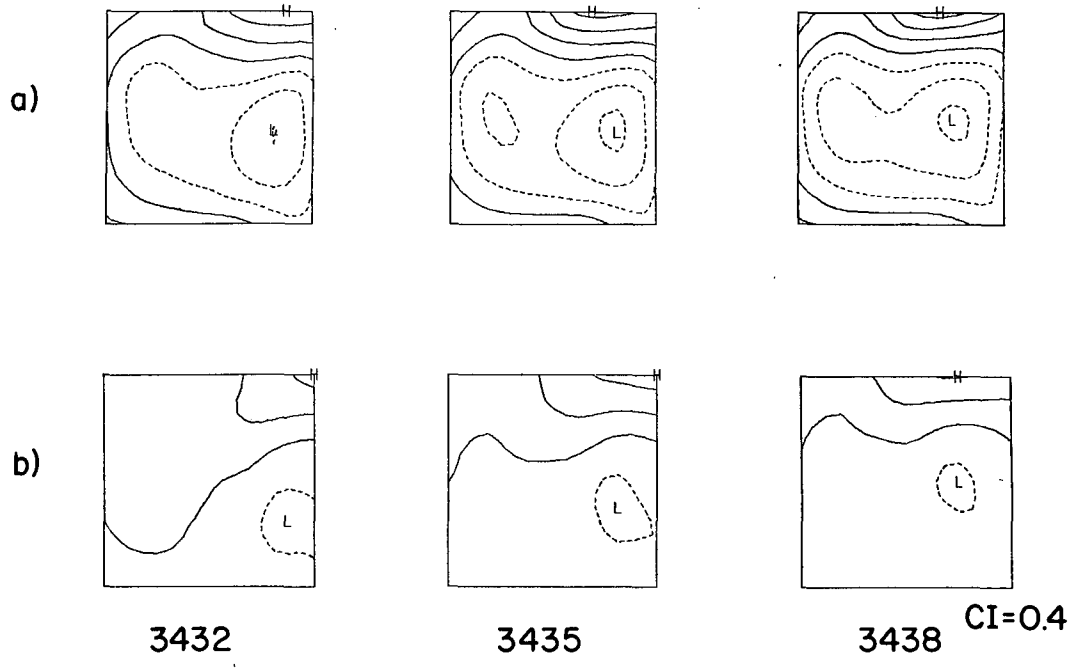

FIG. 9. Difference streamfunction fields at 1400 m for the period 1 forecast. (a) Difference between initial and instantaneous streamfunction at later times inside the forecast experiment, (b) difference between the instantaneous streamfunction and the time-averaged streamfunction between day 3420 and 3450.

m. The vorticity divergences at 1400 meters (Fig. 10b) are dominated by $\langle \Delta F_T \rangle$ which reaches a maximum at day 3440; $\langle \Delta F_R \rangle$ shows a small amplitude wavelike structure with a positive maximum at 3434 and $\langle \Delta F_P \rangle$ is comparable to $\langle \Delta F_R \rangle$.

These behaviors support the conclusion, already evident from the maps, that between days 3430–3440, a translation of the jet and propagation of waves is present at all levels except 1400 m where the baroclinic conversion is occurring. It is also indicative of the complicated vertical structure of the jet–cyclone feature.

The kinetic energy time series (Fig. 10c) shows the onset, development and decay phases of the process in terms of relative maxima in $\langle \Delta F_\pi \rangle$, $\langle \Delta F_K \rangle$, $\langle -b \rangle$ and $\langle \delta f_\pi \rangle$ in the period 3430–3440. This is present at all the levels even though the maxima occur at different times. Before day 3430 at 1400 m, $\langle \Delta F_\pi \rangle$, $\langle \Delta F_K \rangle$ are importing energy in the region of the jet, $\langle -b \rangle$ is converting A into K and $\langle \delta f_\pi \rangle$ is exporting kinetic energy vertically. At the other levels the integrated balances are almost the same except for $\langle \delta f_\pi \rangle$ which imports energy. The $\dot{A}$ time series (Fig. 10d) shows also the onset and decay phases of the process which involves growth of the positive (negative) definiteness of $\langle \Delta F_A \rangle$ ($\langle b \rangle$).

The energy diagram in Fig. 11 shows that the direction of the energy fluxes is consistent with a process of baroclinic instability in the $\dot{A}$ balance but it is mixed in the $\dot{K}$ balance due to the positive contribution of $\overline{\langle \Delta F_\pi \rangle}$, $\overline{\langle \Delta F_K \rangle}$ at 1400 m and only $\overline{\langle \Delta F_K \rangle}$ at the upper levels.

The result is that a perturbation of a smaller spatial scale than the eddy diameter grows in amplitude at the border of the larger eddy via baroclinic conversion. A local strengthening of the jet associated with the large eddy rim is produced along with the development of a small scale cyclone south of the jet. The process of local conversion of A to K from the local temperature gradients is accomplished first at 1400 meters and energy is then exported vertically to the adjacent levels.

b. *Period 3 EVA*

The vorticity terms at 1400 m are shown in Fig. 12. The ΔF_R and ΔF_T are comparable but at different scales and, as before, the former is at smaller scales than the latter. These behaviors are evident also at 700 m while at the two upper levels the major contribution to the local balance comes from ΔF_R. From Fig. 12 we see that at 1400 m, $\dot{T}$ and ΔF_T balance almost perfectly, separately from the relative vorticity terms. After day 3648 the ΔF_R, $\dot{R}$ terms start to dominate the balance and they show an enhanced small wavelike structure together with $\dot{T}$ and ΔF_T. This structure is associated with the jetlike feature invading the domain from the northeastern side. The jet entering the domain has a dynamical balance structure ($\dot{R} \approx \Delta F_R$ locally) very similar to the upper thermocline jet which was present in the region twenty days earlier. The vorticity diver-

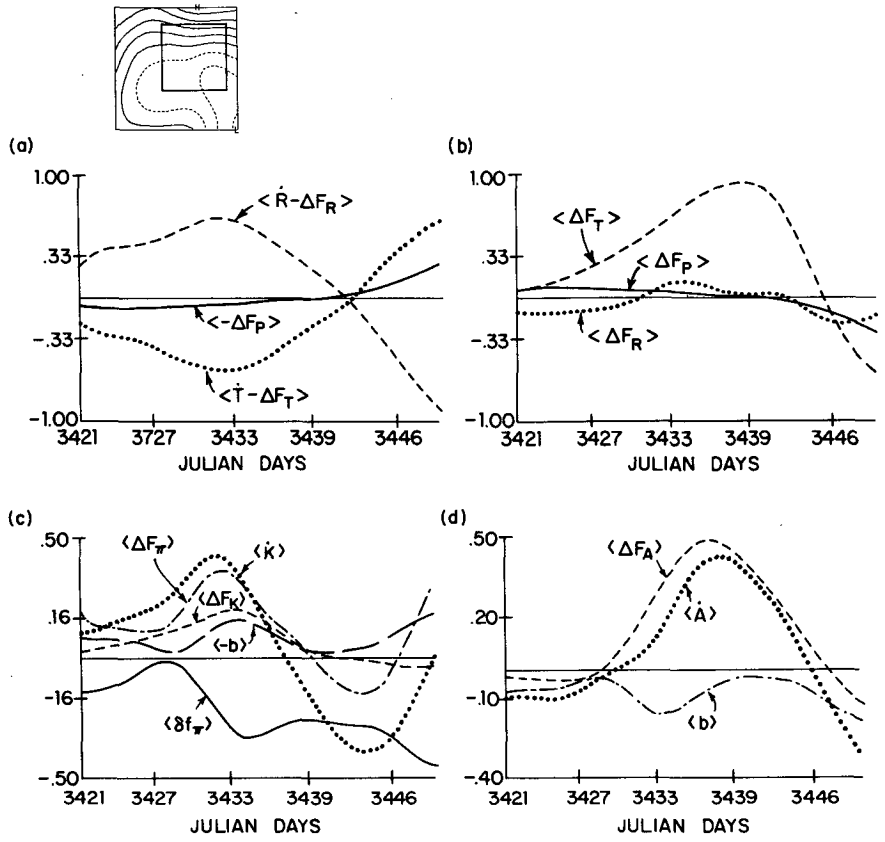

FIG. 10. Integrated vorticity and energy divergences at 1400 m for period 1. The domain of integration is shown in the box at the upper left corner. (a) Vorticity balances, (b) advection of thermal, relative and planetary vorticity, (c) kinetic energy balances, (d) available gravitational energy balances. The symbols are also presented in Table 1.

gences then show a pattern similar to the one observed during Period 1: strong wavelike structures in the relative vorticity terms associated with meandering and strengthening of the jet which also is the border of a larger eddylike feature not contained in the small domain. This time, however, $\dot{T}$ and ΔF_T are more locked in phase than during Period 1, even though they are, as in Period 1, at larger scales than ΔF_R.

The kinetic energy balances are shown in Fig. 13 for the 1400 and 400 m levels. At 400 m (Fig. 13a) the structure of ΔF_K is dipolar and it propagates southward along the jet without remarkable changes in the absolute values of the highs and lows. The ΔF_π exports energy and grows negative definite, achieving a negative maximum around day 3648. Simultaneously at this level δf_π increases its strength, importing energy from adjacent levels. Although not numerically significant at this level, $-b$ starts to convert A into K between 3635–3645.

At 1400 m (Fig. 13b) the ΔF_K term has the same dipolar structure it shows at 400 m, ΔF_π also exports energy between 3638 and 3648. However, at this level δf_π is negative definite and grows asymmetric during the period 3635–3645. The same balance is found at 700 m which (in contrast to Period 1) also exports energy to the adjacent levels. The buoyancy work at 1400 meters is the biggest positive contribution to the $\dot{K}$ balance. Also at 700 meters $-b$ is numerically significant and positive definite. All the components of ΔF_K, ΔF_π and δf_π are important at all levels but δf_π^t and δf_π^a con-

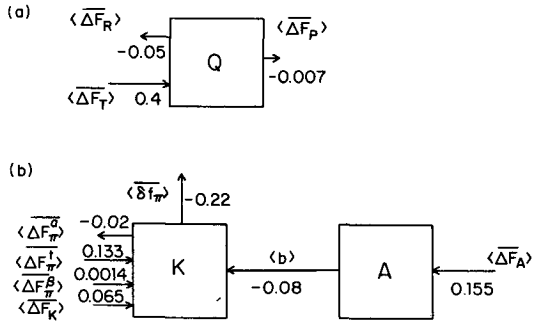

FIG. 11. Diagrams for space and time integrated balances during period 1. The time integral is done over the whole forecast duration and the horizontal average is done in the domain shown in Fig. 9. (a) Vorticity diagrams, (b) energy diagrams.

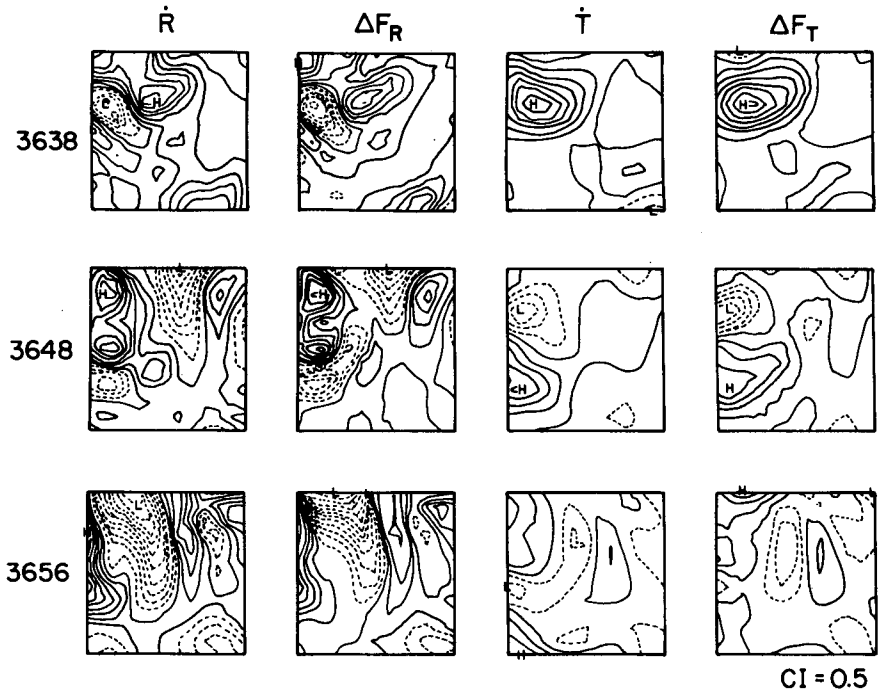

FIG. 12. Instantaneous vorticity balance maps for period 3 forecast. Level 4 at 1400 m.

tributions are dominant at 700 and 1400 m. They are also positive (negative) definite as is typical for baroclinic instability processes (see PR), similarly to Period 1. After day 3648 $\Delta F_\pi{}^t$ becomes one of the major contributions, indicating that, after the baroclinic conversion has happened, enhanced wave propagation takes place.

The A balances (not shown here) display growing asymmetries in ΔF_A at all the levels and b contributes significantly at all the levels to decrease A in the jet region.

The energy and vorticity divergence maps lead to the conclusion that during this period, the process of cyclone intensification and development is triggered by a baroclinic conversion of energy via b which has its maximum at 700 and 1400 m. However, this time the waves have enhanced translation and a shorter spatial scale. This conclusion is reinforced by the difference fields of Fig. 14 which are defined, as before, as the deviations from the initial condition and the "average" state predicted by the model. Figure 14a clearly shows the jet strengthening and cyclone development process inside the domain. It is also evident that this time the spatial scales of the growing perturbation are smaller than during Period 1; Fig. 14b shows the growth of a dypolar wavelike structure along the jet: the high and low centers are approximately 60 km in diameter. Furthermore, the waves seem to have a significant speed of translation with respect to the "average" model state.

The time series of integrated terms are shown in Figs. 15 and 16 for level 2 and 4 at 400 and 1400 m. Level 2 shows an enhanced short time scale wavelike behavior in $\langle \dot{R} - \Delta F_R \rangle$ (Fig. 15a) and the effect of the filter F is quite strong at the beginning and end of the forecast experiment. The main balance is between the vortex stretching terms $\langle \dot{T} - \Delta F_T \rangle$ and $\langle \Delta F_P \rangle$ which contributes significantly to the integrated balance at all levels. Figure 15b clearly shows the short time scale variability of the vorticity divergences. At 100 and 700 m the balance is again between $\langle \dot{T} - \Delta F_T \rangle$ and $\langle \Delta F_P \rangle$. This shows that the local instantaneous balances can be different from the regionally integrated one because of the different spatial scale of the ΔF_R and ΔF_T terms.

At 1400 m (Fig. 16a) the integrated balances are completely reversed and $\langle \dot{R} - \Delta F_R \rangle$ balances $\langle \Delta F_P \rangle$ except during the last part of the forecast from day 3645 to 3660. This integrated balance shows what has been seen qualitatively from the maps: the $\dot{T}$ and ΔF_T contributions cancel between themselves, although the $\langle \Delta F_T \rangle$ term is numerically bigger than $\langle \Delta F_R \rangle$ at this level (see Fig. 16b). The integrated vorticity balance at 1400 meters is reminiscent of the vorticity analysis by Price and Rossby (1982) done in the adjacent LDE region. Their analysis was done for the period following Julian day 3645, after the major baroclinic conversion has occurred in the SDE domain. Their estimated wavelength of 340 km for the planetary barotropic wave indicates that our SDE site could encompass it; a plausible conjecture is that the barotropic wave could have been energized by the process of finite amplitude baro-

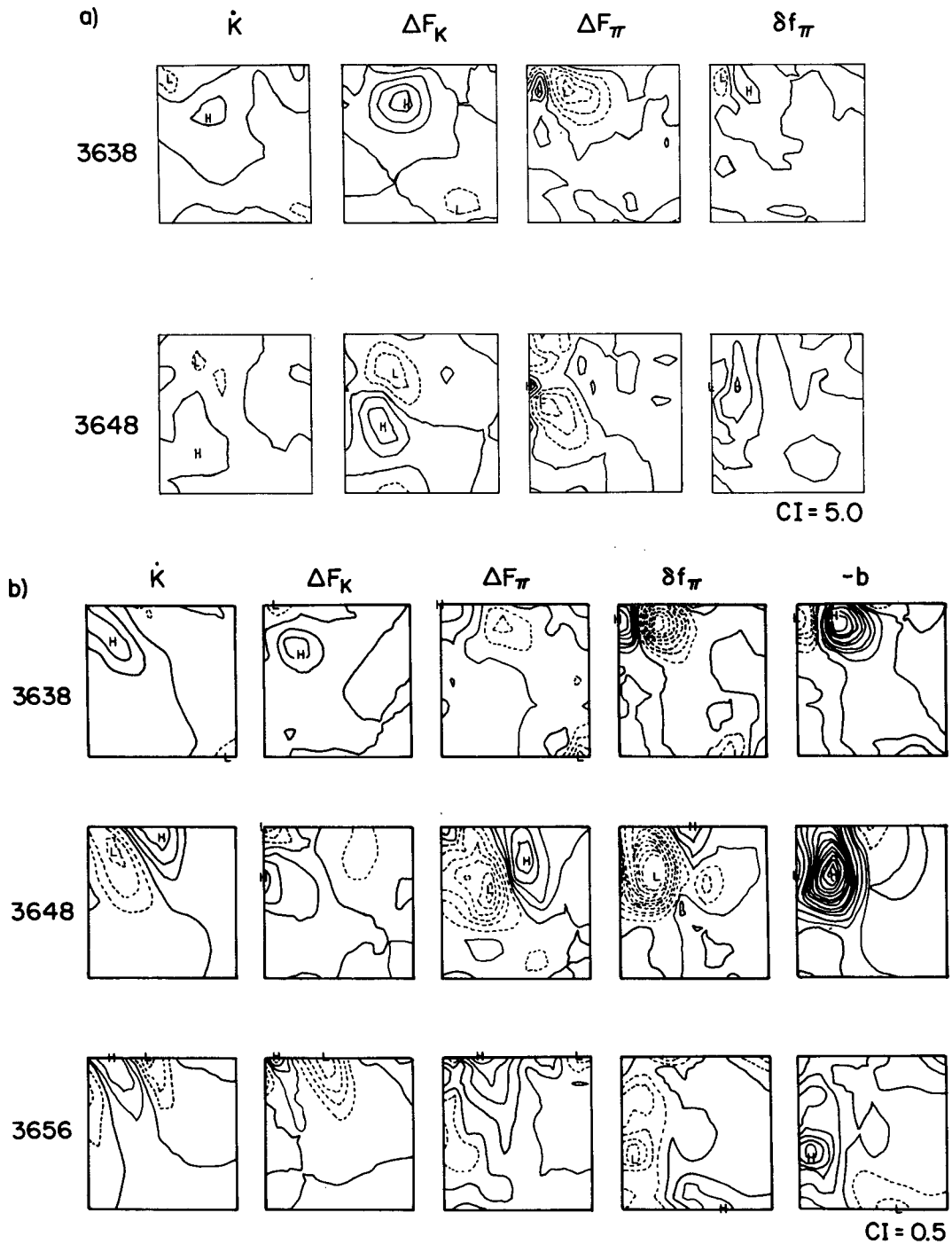

FIG. 13. Kinetic energy balances for Period 3 forecast: (a) 400 m, (b) 1400 m.

clinic conversion of the LDE–SDE jet studied here. Moreover, our vorticity analysis shows that at the upper thermocline levels the integrated vorticity balance is dominated by the thermal vorticity terms and the planetary vorticity advection which is the same as the balance analyzed at the LDE site. The relationship of the SDE jet analyzed here, the LDE jet, and the barotropic wave is pictorially presented by a 500×500 km^2 domain objective mapping analysis performed by Carton and McGillicuddy (1985). The streamfunction map

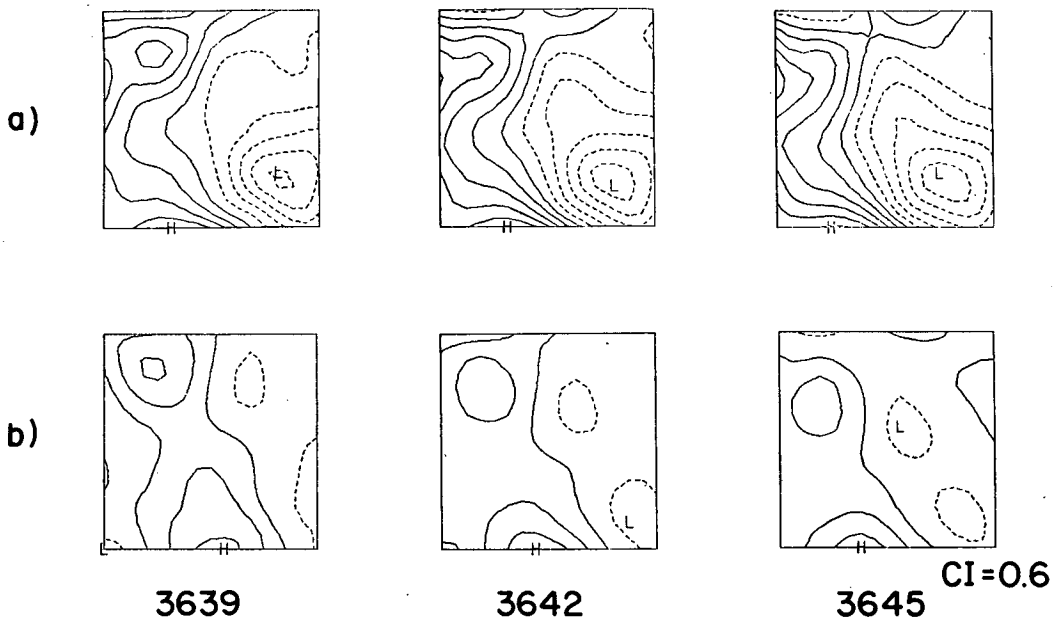

FIG. 14. Streamfunction difference fields for the Period 3 forecast experiment. (a) Difference between initial and instantaneous streamfunction at different times inside the forecast, (b) difference between the "time average" flow and the instantaneous streamfunction of the forecast. The time average is done between days 3630 and 3660.

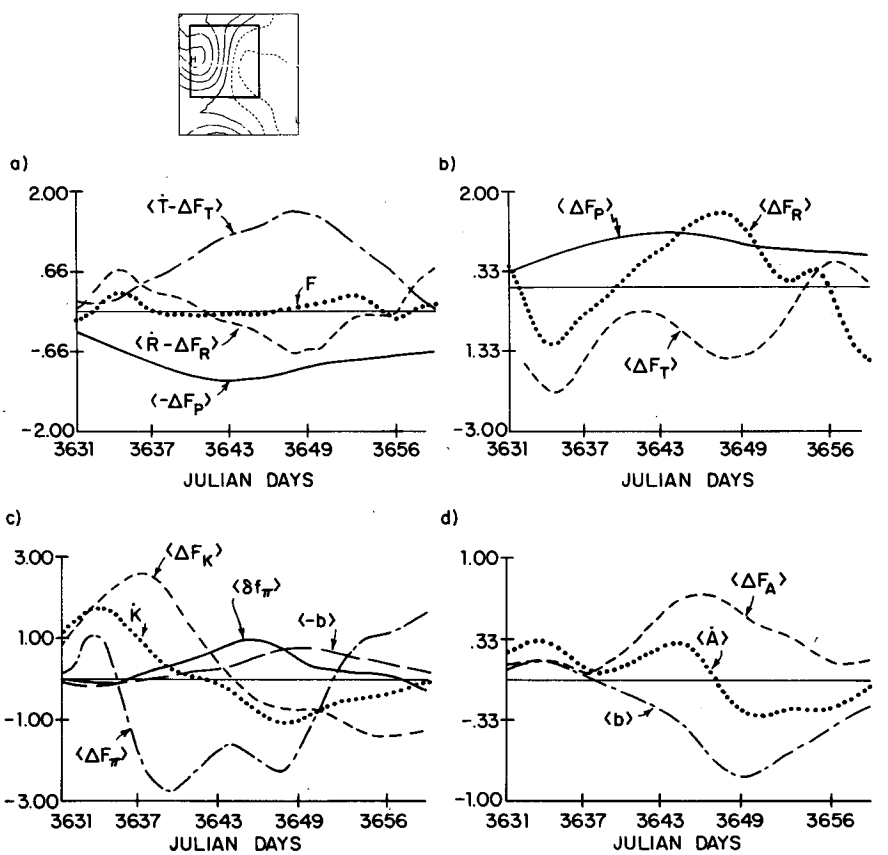

FIG. 15. Vorticity and energy terms time series for Period 3 at 400 m. The domain of integration is shown in the upper left corner map. (a) Vorticity balances, (b) vorticity divergences, (c) kinetic energy balances, (d) available gravitational energy balances.

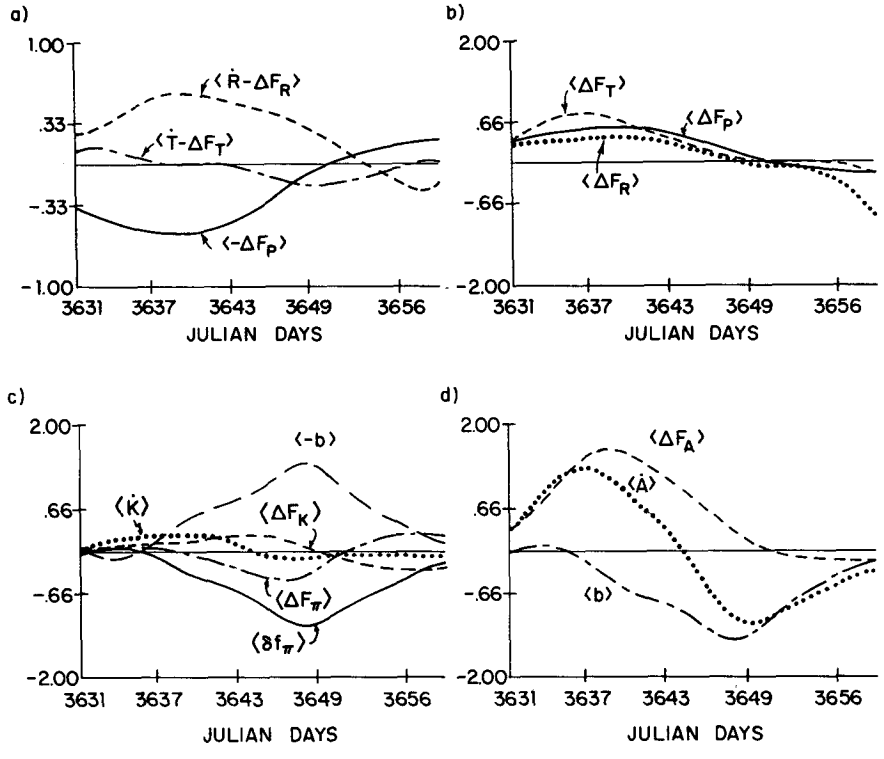

FIG. 16. As in Fig. 15 but for 1400 m.

of Fig. 17 shows the LDE–SDE jet at 1400 m on Julian day 3660 (31 May 1978) extending a downstream distance of at least 200 km with the current meter and SOFAR float vectors superimposed. Figure 4 of McWilliams et al. (1983a) shows the same jetlike feature of the LDE site for different isotherm depths and its picture agrees with the analysis shown in Fig. 17. The SOFAR floats shown in Fig. 2 of Price and Rossby (1982) are clearly trapped in the jet during 10 days (Julian day 3660–3670) of their 60 day oscillation period.

In conclusion, during this period, at 100, 400, 700 m (1400 m) levels the dominant integrated balance is between $\langle \Delta F_T - \dot{T} \rangle (\langle \Delta F_R - \dot{R} \rangle)$ and $\langle \Delta F_P \rangle$, and it is different from Period 1 at 1400 m. The flow has a high amplitude barotropic component at 1400 m but it is highly sheared with respect to the upper thermocline flow. Furthermore, wave propagation effects, as indicated by important contributions from the $\langle \Delta F_P \rangle$ terms, are in this period important during the whole development process. The time series for the $\dot{K}$ and $\dot{A}$ balances show the importance of the vertical transfer and conversion of energy. At 400 m (Fig. 15c) $\langle \Delta F_K \rangle$ imports energy between 3630 and 3640, while $\langle \Delta F_\pi \rangle$ exports it. After day 3640 $\langle \delta f_\pi \rangle$ starts to import energy vertically and $\langle -b \rangle$ reaches a positive maximum. This balance is similar at all the upper thermocline levels. At 1400 m (Fig. 16c) the balance is only between $\langle -b \rangle$ and $\langle \delta f_\pi \rangle$, the first converting A into K and the second exporting K vertically. The sign of $\langle -b \rangle$ and $\langle \Delta F_\pi \rangle$ is in agreement with a process of finite amplitude baroclinic instability and this time the energy dynamics at 1400 m is indicative of a pure baroclinic conversion process in the $\dot{K}$ balance as well. The $\dot{A}$ integrated balances at 400 m and at 1400 m (Fig. 15d and 16d) show the positive definiteness of $\langle \Delta F_A \rangle$ as in the case of a pure baroclinic instability process (see PR).

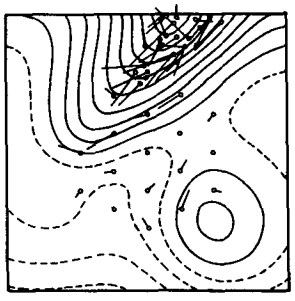

FIG. 17. Streamfunction field at Julian day 3660 for a 500 × 500 km² domain encompassing the LDE and SDE sites. The center of the domain is at 29°N, 70°W. The vectors indicate the SDE and LDE current meters and the Sofar floats. Level at 1400 m. (Reproduced from Carton and McGillicuddy, 1985.)

The energy diagrams for this period are shown in Fig. 18 for 1400 m. The vorticity fluxes are dominated by $\langle \Delta F_P \rangle$ and $\langle \Delta F_T \rangle$, indicating that the thermal vorticity advection is the major nonlinear contribution. The energy diagram shows the pure baroclinic nature

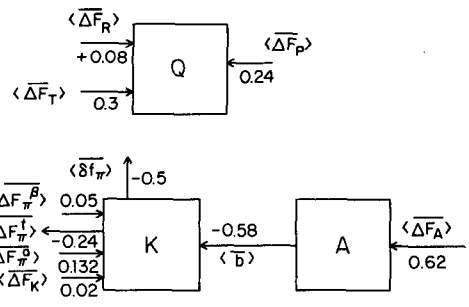

FIG. 18. Vorticity and energy diagrams for the Period 3 forecast experiment. The time integral has been taken from day 3630 until 3660 and the domain of integration in the horizontal is shown in Fig. 15.

of the event very clearly. Note that $\overline{\langle -b \rangle}$ is the major contribution to the net increase of K in the region. As seen in the time series, almost all of $\overline{\langle -b \rangle}$ converted to K is exported vertically via $\overline{\langle \delta f_\pi \rangle}$.

The EVA of this period indicates that the amplifying waves along the sheared flow at the border of larger eddies have very different vertical structure in periods 1 and 3. However, the evident visual analogy between the pressure patterns of Figs. 6a and 6c and the dynamical analysis presented, indicate that the two events are fundamentally the same process; i.e., the local amplification baroclinic waves via conversion of A into K along the temperature gradients at the border of large (compared to the local Rossby radius of deformation) anticyclonic eddies propagating through our domain.

c. *Period 2 EVA*

In Fig. 19 the vorticity balances are shown at 100 and 1400 meters. The balance at the upper thermocline level (Fig. 19a) is between $\dot{R}$ and ΔF_R with neglegible contributions from $\dot{T}$ and ΔF_T. The noticeable feature in this pattern is the very coherent and small scale wavelike pattern of ΔF_R which is also present in the vorticity maps (not shown) as a succession of highs and lows. These small scale features in the divergence field are usually connected with the intense small scale meandering in the pressure pattern which is shown in Fig. 18a. The meridional extent of this "wave packet" in the divergence terms is short and it propagates along the jet southwestward. Level 4 at 1400 m (Fig. 19b) shows, as usual, a more complete balance between all the terms: the ΔF_R, ΔF_T terms have the same scales and this time an important local contribution also comes from the ΔF_P term which is at large scales (the domain scale). Level 2 and 3 are intermediate between the balances at level 1 and 4. The conclusions are that the vorticity dynamics shows enhanced wavelike behaviors, a strong tendency for propagation and the waves have an upper thermocline intensified signature.

In Fig. 20 the kinetic energy balances are only shown for the 1400 meter level. The ΔF_K, ΔF_π terms are at very small scales and are neglegible with respect to the δf_π, $-b$ terms which are negative and positive definite along the jet boarder respectively. While the small scale disturbances in the vorticity divergence maps are propagating, the buoyancy work grows negative definite at the lower thermocline level, converting A to K. The pattern is reminiscent of the normal mode baroclinic instability case discussed in PR. We do not capture the whole process since the jet moves out of our region very rapidly. However, the integrated balances show that there is a net growth of energy at 100 and 400 m due to convergence of kinetic energy via δf_π from 700 and 1400 m where kinetic energy is produced by a net conversion of A into K via b. At 100, 400 and 700 m levels, the integrated vorticity balances (not shown) are different from periods 1 and 3. This time all the terms contribute to the balance: $\langle \dot{T} - \Delta F_T \rangle$ balances $\langle \Delta F_P \rangle$ in the first ten days of the forecast and afterwards $\langle \Delta F_P \rangle$ starts to be balanced by $\langle \dot{R} - \Delta F_R \rangle$. However, at the lower thermocline level, 1400 m, the balance is between $\langle \dot{R} - \Delta F_R \rangle$ and $\langle \Delta F_P \rangle$ as in Period 3. Since the summary diagram for periods 1 and 3 (Figs. 11 and 18) represent space–time averages which we regard as definitive for the processes, we have chosen not to present such diagrams here for the partially captured processes of Period 2.

The conclusions for this period are tentative because of the short duration of the forecast experiment and the rapid movement of the jet out of our domain. The process captured is, however, evident: the jet meanders and strengthens due to the passage of a very short wave disturbance packet which induces a net baroclinic conversion of A to K. The important dynamical difference with the two cases previously discussed is that Rossby wave propagation terms are important even locally and at the deep thermocline levels. However, this period is similar to Period 3 in the dynamical balances and structures of the flow (short spatial scale of the disturbances, importance of the planetary advection terms and highly sheared flow in the thermocline).

7. Conclusions

We have shown a detailed dynamical analysis of the energetics of mesoscale jets and eddy development processes occurring in the POLYMODE SDE area. The methodology of our approach is the same as used to analyze mesoscale dynamics in PR and RCPM. The conceptual framework is described in Robinson and Leslie (1985) and here we apply it to the northwestern Atlantic open ocean regions.

It is shown that the dynamical interpolation via a quasi-geostrophic model is feasible and satisfactorily accurate. Furthermore, it gives results which can be used for dynamical analysis of local mesoscale processes involving strong nonlinear and vertical interactions. We have described the procedures of analysis of XBT

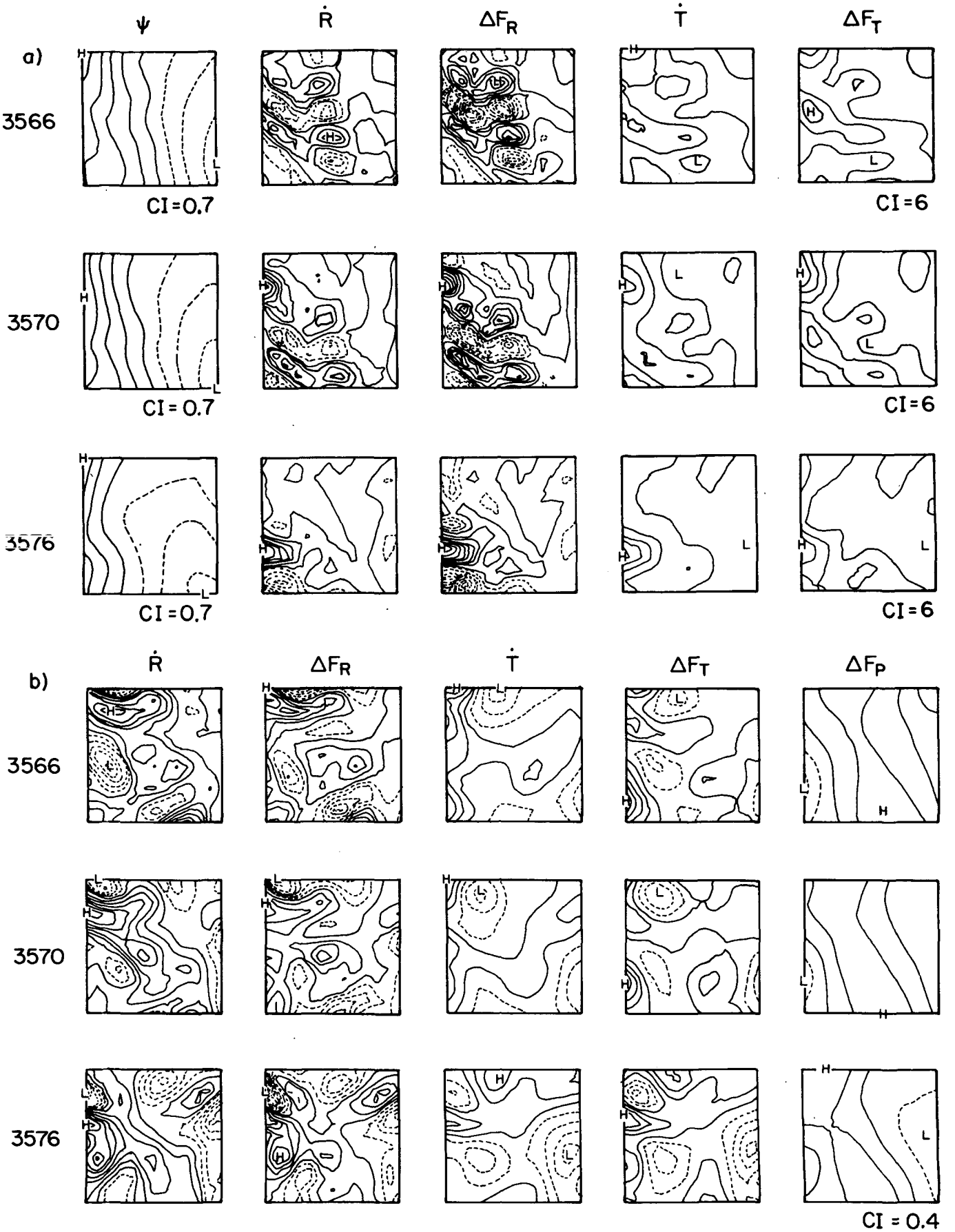

FIG. 19. (a) Pressure (ψ) and vorticity balances at 100 m for the forecast experiment of Period 2. (b) As in (a) but for the 1400 m level.

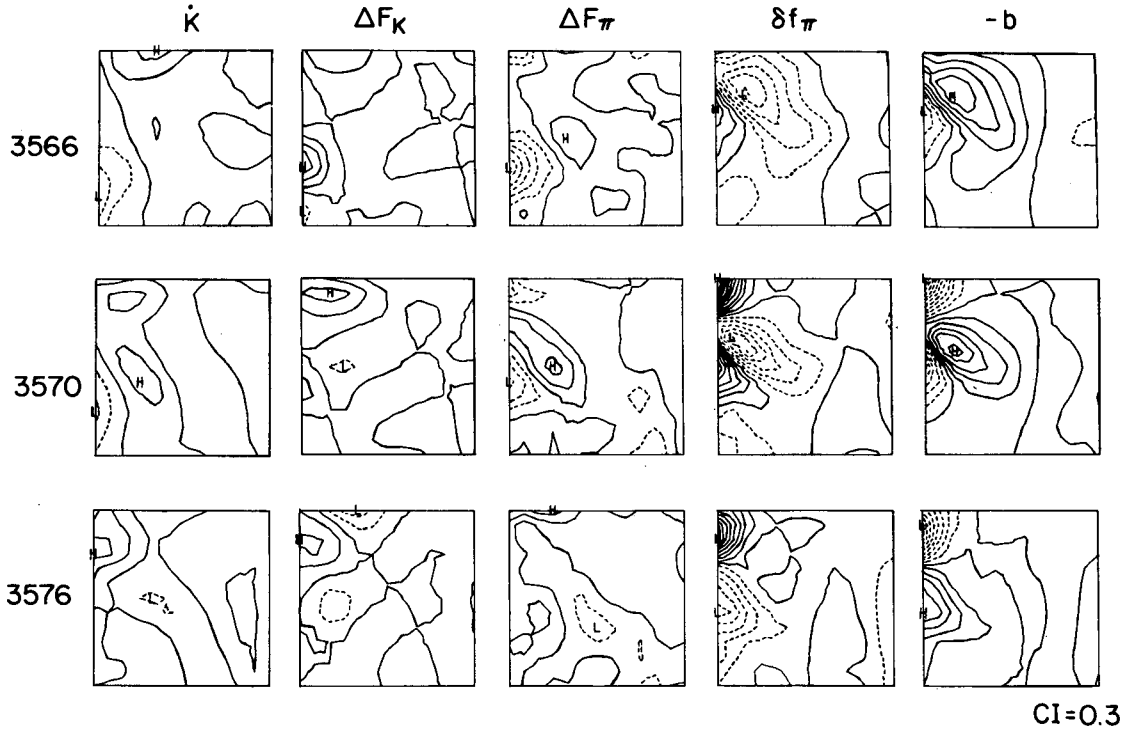

FIG. 20. Kinetic energy balances at 1400 m for the Period 2 forecast. The domain is the same as in Fig. (18).

and current meter data to produce initialization and verification streamfunction fields for the model. The quality of the forecast experiments demonstrate the ability of predicting the evolution of the synoptic/mesoscale variability on the time scale of a month. The forecast experiments are used to elucidate the quantitative local dynamical balances and energetic processes responsible for changes in the deep structure of the midocean eddy field. Even though the domain is relatively small, the model is able to reproduce large changes in the horizontal and vertical structure of the eddy field.

The EVA has been applied as a diagnostic tool in 30- and 20-day forecast experiments and the dynamics are elucidated in terms of the vorticity and energy balances. It is found that, at the southwest extension of the recirculation region of the Gulf Stream system, there exists a local kinetic energy production via baroclinic conversion from available gravitational energy which produces jet meandering, jet intensification and cyclone development at the upper and lower regional thermocline levels. The jets are at the borders of larger eddies which are not resolved by our small domain extension. However, the area of intensification of the jets is considerably smaller than the eddy dimensions and it is contained in the domain examined. The cyclones formed have a diameter of 100–150 km and they are fully contained in the domain.

The three events examined account for most of the variability in the yearlong kinetic energy data series. The temporal width of the events is approximately 30 days. During this length of time, we have local growth of kinetic energy and decay due to export of kinetic energy out of the domain.

In Fig. 21 we show the general schematic of the local frontogenesis and cyclone development process. A large, strong eddy pressure extremum, here described as a high, is paired together with a weaker eddy of opposite sign. A strong jet develops at their mutual border, with the enhancement of both eddies and in particular the formation of a smaller scale cyclone. (Here we have found only large anticyclones at the border of which a cyclonic eddy pressure center develops; however, we cannot exclude generally the possibility of opposite signs). The jet and cyclone formation process is associated with a middle to low thermocline (700–1400) available gravitational to kinetic energy conversion, vertical export of energy from these levels to the upper thermocline (100–400) levels and export of energy via horizontal pressure work divergences at all the levels. Of course, this baroclinic amplification process is mixed to horizontal energy transport mechanisms. Furthermore, at least in two of the three events studied (periods 2 and 3), there is a strong signature of short wave (compared to the Rossby radius of deformation) propagation and in all periods an enhanced advection of these waves along the jet border. The waves travel along the jet and grow in amplitude, extracting energy from the local

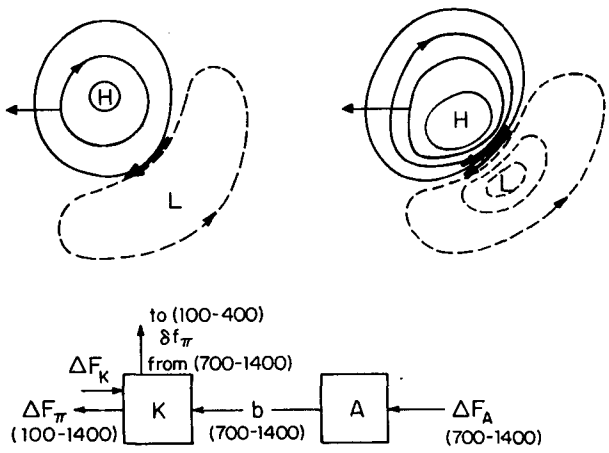

FIG. 21. Schematic representation of the jet–cyclone formation process as seen in the pressure maps. Schematic of the energy conversion and redistribution processes in the jet–cyclone strengthening event. The numbers indicate the vertical levels, and the arrows indicate the direction of the energy flux divergences in or out of the region.

temperature gradient and producing local frontogenesis and cyclone formation. It is interesting to speculate that this growth could be intermittent and common in the open ocean regions even though we observe from a small region and we have captured only a few cycles of this growth which has the time scale of a few weeks.

The role played by nonlinearities is fundamental in both the vorticity and energy balances. The three upper thermocline levels (100, 400, 700 m) show instantaneous balances dominated by relative vorticity terms which are at scales generally smaller than the thermal vorticity terms. The low thermocline level at 1400 m presents a significantly different local balance since both relative and thermal vorticity advections are important. Moreover, the integrated vorticity balances show that the upper thermocline levels are dominated by vortex stretching terms ($\langle \dot{T} - \Delta F_T \rangle$) and planetary vorticity advections, $\langle \Delta F_P \rangle$, even though the $\langle \dot{R} - \Delta F_R \rangle$ terms are intermittently important. At 1400 m the integrated vorticity balances are between $\langle \dot{R} - \Delta F_R \rangle$ and $\langle \Delta F_P \rangle$ with the exception of Period 1.

Periods 1 and 3 seem to be more alike in the development of the baroclinic process even if the vertical structure of the flow field is very different. Both show dipolar structures in the ΔF_K and ΔF_π terms and strong wavelike patterns along the jets. In both cases, energy is imported vertically at the upper thermocline levels from 1400 m where kinetic energy is produced via ΔF_K and b. Period 2 has a prominent wavelike structure in all the terms along the jet line and the waves seem to travel along it relative to the jet translation velocity.

The differences between periods 1 and 3 are in the vertical structure of the jet and in the vertical structure of the cyclone formed at its border. During Period 1 the jet is present at all levels from the initial day; during the first 20 days of Period 3 the jet is strongly upper thermocline intensified in the pressure field and then a jetlike feature invades the domain at 1400 m after the intensification of the jet has already taken place in the upper levels. We relate the upper thermocline jet flow at 100, 400 and 700 m to the jet entering at 1400 m from the northeastern side of the domain 20 days later, since the corresponding local balance in the vorticity equation is similar to that of the existing jet at the upper thermocline. An important difference between periods 1 and 3 resides in the averaged vorticity balances at 1400 meters. Period 1 shows a balance between relative and thermal vorticity terms, while Period 3 is dominated by a balance between relative and planetary vorticity terms. However, the latter is due to an almost perfect balance between $\dot{T}$ and ΔF_T but not to small thermal vorticity advection effects.

The similarities between periods 2 and 3 consist mainly in the enhanced role of ΔF_P in the vorticity balances at all the levels. Also the vertical structure of the field in the two cases is quite similar as discussed in section 3.

The background distribution of jets and cyclonic circulation development is common to all events. The cyclone formed at the rim of the intensified jet seems to be due to the growth of a dipolar structure on the shear at the border of the larger eddies. After the amplification these small cyclonic features move along with the jet and they have also a signature in the subthermocline levels.

In conclusion, the Polymode SDE area presents a spatially inhomogeneous baroclinic environment characterized by large horizontal temperature gradients at the borders of eddy features which are propagating south westward at an average speed of a few centimeters per second. Perturbations are allowed to grow along these eddy borders and develop into intense deep thermocline jets and cyclones via a process typical of baroclinic instability. The spatial scale at which the baroclinic conversion occurs is of the order of 100 km which is comparable to the width of the jet, and the temporal scale is approximately 30 days.

Acknowledgments. The authors wish to thank Mr. Leonard Walstad for help in the preparation of the final dataset used in this analysis. This research was carried out with the support of an Office of Naval Research Grant N00014-84-C-0461.

REFERENCES

Atlas of the Mid-Ocean Dynamics Experiment (MODE-I), 1977: M.I.T. Cambridge Mass.

Bogden, P. S., 1983: The mesoscale temperature variability in the Western North Atlantic. Honor's thesis, Harvard University.

Bryden, H. L., 1982: Sources of eddy energy in the Gulf Stream recirculation region. *J. Mar. Res.*, **40**(Suppl), 509–524.

——, and N. P. Fofonoff, 1977: Horizontal divergence and vorticity estimates from velocity and temperature measurements in the Mode region. *J. Phys. Oceanogr.*, **7**, 329–337.

Carter, E. F., 1983: The statistics and dynamics of ocean eddies. Ph.D. thesis, Harvard University.

——, and A. R. Robinson, 1986: Analysis models for the estimation of oceanic fields. *J. Atmos. Oceanic Technol.* **4,** 49–74.

Carton, J. A., and D. J. McGillicuddy, 1985: Comprehensive objective maps of POLYMODE streamfunction. Harvard Open Ocean Model Reports, 21. Harvard University, Division of Applied Sciences, Cambridge, Massachusetts.

Fofonoff, N. P., and R. C. Millard Jr., 1983: Algorithms for oceanic computations.

Heinmiller, R. H., 1983: Instruments and Methods. *Eddies in Marine Science.* A. R. Robinson, Ed. Springer-Verlag, 542–567.

Hua, B. L., J. C. McWilliams and W. B. Owens, 1986: An objective analysis of the POLYMODE Local Dynamics Experiment. Part II: Streamfunction and potential vorticity fields during the intensive period. *J. Phys. Oceanogr.,* **16,** 506–522.

McWilliams, J. C., 1976: Maps from the Mid-Ocean Dynamics Experiment. Part II. Potential vorticity and its conservation. *J. Phys. Oceanogr.,* **6,** 828–846.

——, et al., 1983a: The local dynamics of eddies in the Western North Atlantic. *Eddies in Marine Science,* A. R. Robinson, Ed. Springer-Verlag, 92–112.

——, 1983b: On the mean dynamical balances of the Gulf Stream Recirculation zone. *J. Mar. Res.,* **41,** 427–460.

——, W. B. Owens and B. L. Hua, 1986: An objective analysis of the POLYMODE Local Dynamics Experiment. Part I: General formalism and statistical model selection. *J. Phys. Oceanogr.,* **16,** 483–504.

Miller, R. N., A. R. Robinson and D. B. Haidvogel, 1983: A baroclinic quasigeostrophic open ocean model. *J. Comput. Phys.,* **50,** 38–70.

Mode Group, 1978: The Mid-Ocean Dynamics Experiment. *Deep-Sea Res.,* **25,** 859–910.

Owens, W. B., J. R. Luyten and H. L. Bryden, 1982: Moored velocity measurements on the edge of the Gulf Stream recirculation. *J. Mar. Res.,* **40**(Suppl), 509–524.

Polloni, C., A. Mariano and T. Rossby, 1981: Streamfunction maps of the polymode current meters array. U.R.I. Tech. Rep. mp/81-1/Mode Contribution No. 36-T.

Price, J. F., and H. T. Rossby, 1982: Observations of a barotropic planetary wave in the Western North Atlantic. *J. Mar. Res.,* **40**(Suppl), 543–558.

Pinardi, N., and A. R. Robinson, 1986: Quasigeostrophic energetics of open ocean regions. *Dyn. Atmos. Ocean,* **10,** 185–221.

Robinson, A. R., 1982: Dynamics of ocean currents and circulation: results of Polymode and related investigations, *Topics in Ocean Physics, Societa' italiana di Fisica,* A. Osborne and P. M. Rizzoli, Ed., Bologna, Italy.

——, and W. G. Leslie, 1985: Estimation and prediction of oceanic eddy fields. *Progress in Oceanography,* Vol. 14, Pergamon, 485–510.

——, J. A. Carton, N. Pinardi and C. N. K. Mooers, 1986: Dynamical forecasting and dynamical interpolation: an experiment in the California Current. *J. Phys. Oceanogr.,* **16,** 1561–1579.

Shapiro, R., 1970: Smoothing, filtering and boundary effects. *Rev. Geophys. Space Phys.,* **8,** 358–387.

Shen, C. Y., J. C. McWilliams, B. A. Taft, C. C. Ebbesmeyer and E. J. Lindstrom, 1986: The mesoscale spatial structure and evolution of dynamical and scalar properties observed in the Northwestern Atlantic Ocean during the POLYMODE Local Dynamics Experiment. *J. Phys. Oceanogr.,* **16,** 454–482.